AP-1 transcription factor network explains diverse patterns of cellular plasticity in melanoma

Natacha Comandante-Lou [1,2,5], Douglas G. Baumann [1,4,5], Mohammad Fallahi-Sichani [1,3,6,*]

[1] Department of Biomedical Engineering, University of Virginia, Charlottesville, VA 22908, USA

[2] Department of Biomedical Engineering, University of Michigan, Ann Arbor, MI 48109, USA

[3] UVA Cancer Center, University of Virginia, Charlottesville, VA 22908, USA

[4] Present address: Dewpoint Therapeutics, 451 D Street, Suite 104, Boston, MA 02210

[5] These authors contributed equally

[6] Lead Contact

[*] Correspondence: fallahi@virginia.edu

Summary

Cellular plasticity associated with fluctuations in transcriptional programs allows individual cells in a tumor to adopt heterogeneous differentiation states and switch phenotype during their adaptive responses to therapies. Despite increasing knowledge of such transcriptional programs, the molecular basis of cellular plasticity remains poorly understood. Here, we combine multiplexed transcriptional and protein measurements at population and single-cell levels with multivariate statistical modeling to show that the state of AP-1 transcription factor network plays a unifying role in explaining cellular plasticity in melanoma. We find that a tightly regulated balance between AP-1 factors cJUN, FRA2, FRA1 and cFOS determines the intrinsic diversity of differentiation states and adaptive responses to MAPK inhibitors in individual melanoma cells. Perturbing this balance through genetic depletion of specific AP-1 proteins, or by MAPK inhibitors, shifts cellular heterogeneity in a predictable fashion. Thus, AP-1 may serve as a critical node for manipulating cellular plasticity with potential therapeutic implications.

Keywords

AP-1 transcription factors, differentiation state heterogeneity, cellular plasticity, single-cell analysis, computational modeling, statistical learning, BRAF-mutant melanoma, MAPK signaling pathway, targeted therapies, adaptive drug resistance

Introduction

Individual cells, even those derived from the same clone, respond heterogeneously to environmental perturbations (Mitchell and Hoffmann, 2018; Munsky et al., 2012). Nongenetic heterogeneity can arise due to variances associated with transcriptional state plasticity (Battich et al., 2015; Gupta et al., 2011; Munsky et al., 2012; Symmons and Raj, 2016). Although such plasticity is required for the proper development of complex organisms (Arias and Hayward, 2006), it limits the efficacy of therapies that target abnormally-activated signaling pathways (Boumahdi and de Sauvage, 2020; Sharma et al., 2010). An example of cell-to-cell transcriptional heterogeneity with phenotypic consequences for therapy resistance is observed in melanomas (Emert et al., 2021; Fallahi□Sichani et al., 2017; Shaffer et al., 2017). Numerous studies have associated fluctuations in the state of MAPK inhibitor sensitivity across BRAF-mutant melanoma cells to intrinsic variations in their differentiation state (Baron et al., 2020; Belote et al., 2021; Khaliq et al., 2021; Rambow et al., 2018; Tsoi et al., 2018; Wouters et al., 2020). The reported heterogeneity spans a range of transcriptionally distinguishable states, including a relatively drug-sensitive, melanocytic phenotype that expresses melanocyte lineage markers SOX10 and MITF (Lin and Fisher, 2007), to less drug-sensitive states, including neural crest-like cells that express NGFR (Fallahi□Sichani et al., 2017; Mica et al., 2013), and undifferentiated cells characterized by the overexpression of AXL and loss of SOX10 and MITF (Konieczkowski et al., 2014; Müller et al., 2014). In addition to intrinsic disparities in differentiation state, drug-induced adaptive responses may help a fraction of cells rewire their state of MAPK inhibitor sensitivity, most commonly through dedifferentiation (concomitant with loss of MITF and acquisition of NGFR) (Fallahi□Sichani et al., 2017; Marin-Bejar et al., 2021; Rambow et al., 2018) or reactivation of the MAPK pathway (Gerosa et al., 2020; Lito et al., 2012). Although the emergence and consequences of such intrinsic and adaptive heterogeneities are widely recognized, there is still more to learn about their origins and their possible

connection at a molecular level. For example, it is unclear whether these seemingly distinct forms of heterogeneity arise from independent mechanisms, or whether the observed variability in the initial state of cells and their adaptive changes following MAPK inhibitor treatment could both be traced back to a common subset of molecular players.

Transcription factor networks that regulate the expression of genes in response to signaling pathway perturbations play a key role in creating the biological noise that leads to population heterogeneity (Huang, 2009; Pedraza and van Oudenaarden, 2005). The AP-1 protein family comprises one such network that serves as a major transcription node, integrating inputs from the upstream MAPK signaling pathway (Karin, 1995). In addition to linking signal transduction to transcription, AP-1 proteins have been recently identified to serve as pioneer factors, establishing chromatin states that predispose cells to transcriptional programs driven by other transcription factors or histone modifications, thereby guiding cells towards paths of differentiation or epigenetic reprogramming (Madrigal and Alasoo, 2018; Martínez-Zamudio et al., 2020; Phanstiel et al., 2017; Vierbuchen et al., 2017). These roles are consistent with numerous reports on AP-1 proteins being involved in resistance to MAPK inhibitors, cell state heterogeneity, and therapy-induced dedifferentiation in melanomas and other cancers (Emmons et al., 2019; Fallahi-Sichani et al., 2015; Fallahi□Sichani et al., 2017; Haas et al., 2021; Johannessen et al., 2013; Kong et al., 2017; Maurus et al., 2017; Ramsdale et al., 2015; Riesenberg et al., 2015; Torre et al., 2021; Wouters et al., 2020). Despite these reports, we lack a clear understanding of the rules that define AP-1 behavior and its role in explaining the intrinsic plasticity and the diversity of adaptive responses to MAPK signaling perturbations. This gap in our knowledge may be addressed by a system-wide analysis with single-cell precision to reveal interdependencies between an array of AP-1 proteins, which comprise over a dozen transcription factors, including JUN, FOS, and

ATF subfamilies (Rodríguez-Martínez et al., 2017), their post-translational modification states, and their association with melanoma cell phenotypes at a single-cell level.

In this paper, we test the hypothesis that the state of the AP-1 transcription factor network determines the intrinsic diversity of phenotypic states (i.e., differentiation states) and adaptive responses to MAPK inhibitors in BRAF-mutated melanoma cells. We define the AP-1 state as the combinatorial concentrations of AP-1 proteins, their phosphorylation state, and their transcriptional activity, which are either measurable experimentally, or inferable by using bioinformatics tools. Our systems biology approach combines multiplexed measurements of the AP-1 state, MAPK signaling activity and differentiation state, at population and single-cell levels, across many genetically characterized melanoma cell lines before and after their exposure to BRAF/MEK inhibitors. We apply statistical learning to capture the predictivity of AP-1 states, and corresponding AP-1 factors, for phenotypic heterogeneity in melanoma cultures and patient-derived tumors. We then employ RNAi-mediated knockdown experiments combined with single-cell analysis to validate the causality of our statistical predictions in a heterogeneous melanoma cell population. We find that a tightly regulated balance between AP-1 transcription factors cJUN, FRA2, FRA1 and cFOS and their transcriptional activity determines the baseline differentiation state of melanoma cells. This balance is perturbed following MAPK pathway inhibition. Nevertheless, MAPK-inhibitor-induced changes in the AP-1 state, including the abundance of cJUN and its phosphorylation, as well as the phosphorylation state of FRA1, remain strong predictors of drug-induced dedifferentiation and adaptive MAPK pathway reactivation, respectively. These results show that the state of AP-1 network offers a critical context, which controls not only the initial state of melanoma cells and their population heterogeneity, but also their adaptive changes immediately following MAPK pathway inhibition. Thus, AP-1 may serve as a critical node for strategies to manipulate cellular plasticity in melanoma with potential therapeutic implications.

Results

Single-cell AP-1 protein levels predict differentiation state heterogeneity in melanoma cells

To quantify the baseline heterogeneities in differentiation state and to assess their covariation with AP-1 proteins across genetically diverse or isogenic melanoma cell populations, we utilized an iterative indirect immunofluorescence imaging (4i) protocol (Gut et al., 2018) in conjunction with high-throughput automated microscopy (Figure 1A). We multiplexed measurements of 21 proteins using 4i-validated antibodies in 19 BRAF-mutant melanoma cell lines (Figure 1B). The measurements included total levels of eleven AP-1 transcription factors (including cFOS, FRA1, FRA2, cJUN, JUNB, JUND, ATF2, ATF3, ATF4, ATF5 and ATF6), six AP-1 phosphorylation states (including p-cFOS^{S32}, p-FRA1^{S265}, p-cJUN^{S73}, p-ATF1^{S63}, p-ATF2^{T71} and p-ATF4^{S245}) and four differentiation state markers MITF, SOX10, NGFR and AXL. Importantly, these four differentiation state markers were previously reported to represent transcriptionally distinct melanoma differentiation states (Khaliq et al., 2021; Tsoi et al., 2018). The panel of 19 melanoma cell lines tested represented a broad spectrum of differentiation states, including populations of melanocytic (MITF^{High}/SOX10^{High}/NGFR^{Low}/AXL^{Low}), transitory (MITF^{High}/SOX10^{High}/NGFR^{High}/AXL^{Low}), neural crest-like (MITF^{Low}/SOX10^{High}/NGFR^{High}/AXL^{High}) and undifferentiated (MITF^{Low}/SOX10^{Low}/NGFR^{Low}/AXL^{High}) cells (Figures 1C, 1D). We and others have shown that the frequency of these states in melanoma cell populations varies from one tumor to another and predicts their overall sensitivity to MAPK inhibitors (Khaliq et al., 2021; Rambow et al., 2018; Tirosh et al., 2016). Here, we asked whether the observed heterogeneities in differentiation state could be explained by variations in patterns of AP-1 measurements at a single-cell level.

The population-averaged and single-cell protein data revealed a high degree of variation in differentiation state markers and AP-1 proteins across genetically distinct cell lines (Figures 1B, 1C, S1). To test whether there is a relationship between AP-1 variations and the differentiation state of individual cells regardless of their genetic differences, we randomly sampled a total of 10,000 cells, including 2,500 from each of the four differentiation states, in a way that they represented all 19 cell lines and 4 distinctive differentiation states as equally as possible (Figure 1D). We used the multiplexed AP-1 data of 80% of the cells to train a random forest classification model to predict the differentiation state of each individual cell. We then used the remaining 20% of the cell population to independently validate model predictions. Model-predicted single-cell differentiation states matched true (measured) differentiation states with an accuracy of 0.74, representing a remarkable performance relative to a random 4-class classifier with an expected accuracy of 0.25 (Figure 1E). A close look at model predictions showed that they matched true states for ~88% of undifferentiated cells, ~72% of neural crest-like cells and >66% of melanocytic cells. In cases where the true and predicted state of a cell did not match, the model predicted a closely related neighboring state along the differentiation state trajectory. When we combined cells from these related states, e.g., cells in melanocytic and transitory states, the model was able to distinguish them from the other two states with an accuracy of >90% (Figure 1E).

To identify those AP-1 measurements that most strongly predicted single-cell differentiation state, we computed the SHapley Additive exPlanations (SHAP) values for the random forest classifications (Lundberg et al., 2020). SHAP assigns each AP-1 factor an importance value, quantifying its contribution, either positively or negatively, to the predicted differentiation state of any given cell (Figure 1F). Among the most important AP-1 factors (ranked based on mean absolute SHAP values) were p-cFOS, FRA2, ATF4, cFOS, p-FRA1 and cJUN. Single-cell measurements of these six factors

made it possible to predict the differentiation state of a cell with an accuracy of 67% (Figure 1G). In agreement with the SHAP analysis results, dimensionality reduction by Uniform Manifold Approximation and Projection (UMAP) (Becht et al., 2018) using only the top six AP-1 factors resulted in a continuous trajectory ordered from melanocytic to undifferentiated states (Figures 1H, 1I). Together, these analyses revealed that the heterogeneity in melanoma differentiation state was associated with distinguishable patterns of variation in the expression of a few key AP-1 proteins. Melanocytic and transitory cells expressed substantially higher levels of p-cFOS, cFOS and ATF4, while undifferentiated cells exhibited lower levels of all these factors and instead exhibited increased levels of FRA2, cJUN and p-FRA1.

AP-1 transcript levels predict variations in differentiation state programs across melanoma lines

To test whether the relationships between the patterns of AP-1 expression and melanoma differentiation state were recapitulated at the transcriptional level, we analyzed a previously published dataset, including RNA sequencing of 53 melanoma cell lines (Tsoi et al., 2018). Each cell line was assigned a series of seven signature scores, defined as the average of z-scores for the expression levels of differentiation state signature genes (Tsoi et al., 2018). The differentiation signature scores were then related to the transcript levels of 15 AP-1 genes for each cell line by partial least square regression (PLSR) (Figure 2A). The overall performance of the PLSR model was evaluated by computing the fraction of variance in signature scores explained (R^2) or predicted (Q^2) by changes in AP-1 gene expression (Figure 2B). The model revealed a high performance and prediction accuracy with R^2 of 0.72 and Q^2 of 0.55 (using leave-one-out cross-validation) for four PLSR components. To evaluate the accuracy of predictions for each differentiation state, we assessed the correlation between the signature scores derived from the differentiation signature genes and scores predicted by the PLSR model. The

model showed consistent accuracy with an average Pearson's correlation coefficient of 0.74 ± 0.08 (P = 3.2×10^{-17} to 1.3×10^{-6}) between the actual and predicted signature scores (Figure 2A). To independently validate the model predictions, we used RNA sequencing data from a different panel of 32 BRAF-mutant melanoma cell lines in the Cancer Cell Line Encyclopedia (CCLE) (Ghandi et al., 2019). The PLSR model trained against the original set of 53 cell lines was able to predict the differentiation signature scores in the new set of 32 melanoma cell lines, leading to an average Pearson's correlation coefficient of 0.65 ± 0.13 (P = 2.3×10^{-8} to 6.8×10^{-3}) between the actual and predicted scores (Figure 2C).

The high performance of the PLSR model shows that variations in the transcriptional levels of at least some AP-1 genes may explain the variability in differentiation states across melanoma cell lines. In agreement with this expectation, different cell lines could be separated by their PLSR scores based on their position along the different state trajectory (Figure 2D). Because the PLSR model achieved its maximum prediction accuracy by four components, we computed the Variable Importance in the Projection (VIP) scores across all these components to determine the overall contribution of each AP-1 gene to each differentiation state (Figure 2E). Among the most important predictors of differentiation state (determined by |VIP| > 1) were the expression of FOS (encoding cFOS), FOSL1 (encoding FRA1), FOSL2 (encoding FRA2), JUN (encoding cJUN), JUNB, JUND, ATF2 and ATF4 (Figure 2E). Importantly, a model created using only these AP-1 genes was able to significantly outperform most PLSR models that were built based on combinations of eight randomly chosen transcription factors from the basic leucine zipper (bZIP) family (the family to which AP-1 factors belong) (P = 0.008) or based on any eight randomly chosen transcription factors (P = 0.01) (Figure 2F).

Together, these analyses revealed that the predictivity of patterns of AP-1 variation for melanoma differentiation state could also be captured at the level of transcription of these factors. Except for ATF4, the statistical association of AP-1 factors with differentiation state was generally

consistent across bulk transcript and single-cell protein measurements. Melanocytic and transitory cells expressed substantially higher levels of FOS transcript and cFOS protein levels, whereas undifferentiated cells were associated with increased levels of FOSL1, FOSL2 and JUN transcripts and their corresponding proteins FRA1, FRA2 and cJUN, respectively.

Single-cell network inference reveals the role of AP-1 activity in regulation of differentiation programs

Next, we asked whether the statistical associations between the identified key AP-1 proteins and single-cell differentiation states resulted from the active regulation of differentiation programs by the AP-1 factors. To address this question, we applied single-cell regulatory network inference and clustering (SCENIC) (Aibar et al., 2017; Van de Sande et al., 2020) to analyze a previously published single-cell RNA sequencing dataset of 10 melanoma cell lines (Wouters et al., 2020). SCENIC uses single-cell gene expression data to infer transcription factors alongside their candidate target genes (collectively called a regulon), enabling the identification of regulatory interactions and transcription factor activities with high confidence. Enrichment analysis of differentiation signature genes among 10 cell lines showed that they predominantly consisted of cells in the melanocytic, transitory, or undifferentiated states. In line with our results from the gene and protein expression analyses, SCENIC analysis found the FOSL2 and JUN motif regulons to be substantially enriched in populations of undifferentiated cells in comparison with melanocytic or transitory cells (Figures 3A, 3B). The activity of the FOSL1 regulon was low in melanocytic cells but gradually increased among transitory and undifferentiated cells (Figure 3C). The FOS regulon, on the other hand, was substantially enriched in melanocytic and transitory cells, but its activity was low in undifferentiated cells (Figure 3D).

To test whether the relationship between AP-1 regulon activities and melanoma differentiation states existed in single cells derived from tumor biopsies, we performed differentiation state enrichment and SCENIC analysis on single-cell RNA sequencing data previously collected via dissociation and profiling of patient-derived melanoma samples (Jerby-Arnon et al., 2018; Tirosh et al., 2016). Enrichment analysis of differentiation signature genes among 11 treatment-naïve malignant melanoma samples showed that they consisted of cells in either melanocytic or undifferentiated states. In agreement with the analysis results from the established melanoma cultures, SCENIC analysis of patient tumors showed that FOSL2, JUN and FOSL1 regulons were significantly enriched in undifferentiated cells in comparison with melanocytic cells (Figures 3E-3G). In contrast to a substantially higher FOS regulon activity observed in cultured melanocytic cells, the activity of FOS regulon was only slightly higher in melanocytic tumor cells in comparison with undifferentiated cells (Figure 3H). Interestingly, however, the FOS/JUN activity ratio at a single-cell level was able to distinguish melanocytic cells from undifferentiated cells more efficiently than either of these AP-1 factors alone (Figure 3I), suggesting that it is the balance between AP-1 factor activities that determines a cell's differentiation state. Together, these analyses revealed that melanoma cells of diverse differentiation states are associated with distinct regulatory network activities by AP-1 transcription factors. In particular, the role of FOS, FOSL1, FOSL2 and JUN regulon activities was consistent with their corresponding patterns of gene and protein expression across melanoma differentiation states at both population and single-cell levels.

MAPK inhibitor-induced changes in the AP-1 state predict patterns of drug-induced dedifferentiation and ERK pathway reactivation

Although melanoma populations consist of stable mixtures of cells in diverse differentiation states at baseline, they can switch state in response to environmental perturbations. Treatment with MAPK

inhibitors, for example, may induce the dedifferentiation of melanocytic cells toward the neural crest-like phenotype. Such adaptive phenotype switching occurs as early as 2-3 days of exposure to MAPK inhibitors, concomitantly with loss of MITF and acquisition of NGFR (Khaliq et al., 2021). In addition to drug-induced dedifferentiation, adaptive reactivation of the ERK pathway following a transient period of ERK inhibition is known as a common mechanism of adaptive resistance that helps tumor cells escape the effect of drug (Gerosa et al., 2020; Lito et al., 2012). To determine common patterns of AP-1 changes that might be associated with these adaptive responses, we exposed 18 BRAF-mutant cell lines to the BRAF inhibitor vemurafenib (at 0.316 µM) either alone or in combination with the MEK inhibitor trametinib (at 0.0316 µM). We fixed the cells following 24 or 72 h of treatment and then used the 4i procedure to measure the abundance or phosphorylation state of AP-1 transcription factors, MITF, NGFR, and p-ERK$^{T202/Y204}$ (Figures 4A, S2-S3).

To identify possible associations between AP-1 factors and drug-induced dedifferentiation, we first calculated the relative enrichment of dedifferentiated cells at baseline (DMSO) or following MAPK inhibitor treatments by subtracting the fraction of cells that are NGFR^{Low}/MITF^{High} from the fraction of cells that are NGFR^{High}/MITF^{Low}. We then used pairwise partial correlation analysis to reveal statistical associations between each of the AP-1 measurements and the enrichment of dedifferentiated cells following MAPK inhibitor treatments across 18 cell lines, while controlling for the intrinsic (drug-naïve) variance in the enrichment of dedifferentiated cells across cell lines (Figure 4B). This analysis identified cJUN and p-cJUN as the strongest predictors of drug-induced dedifferentiation in melanoma cells following 72 h of exposure to either of the MAPK inhibitors (Figure 4C). In agreement with population-level correlation analysis, single-cell analysis revealed significant increases in cJUN and p-cJUN levels of melanoma cells that switched from an NGFR^{Low}/ MITF^{High} state to an NGFR^{High}/ MITF^{Low} state following drug treatment (Figure 4D).

We then asked which, if any, of AP-1 factors might capture drug-induced adaptive changes in ERK signaling. Consistent with previous data (Gerosa et al., 2020), treatment of cells with vemurafenib at 0.316 μM strongly suppressed the average p-ERK levels within 24 h in all cell lines (Figure 5A). Each cell line, however, showed long-tailed single-cell distributions of p-ERK level, indicating significant cell-to-cell heterogeneity in ERK pathway inhibition. Over the following 48 h of vemurafenib treatment (i.e., t = 72 h), p-ERK levels were further elevated because of adaptive reactivation of ERK signaling (Figure 5A). Cells treated with the combination of vemurafenib (at 0.316 μM) and trametinib (at 0.0316 μM), however, exhibited reduced p-ERK levels in comparison with cells treated with vemurafenib alone for either 24 or 72 h (Figure 5A). To assess if any of the AP-1 factors would capture such time-dependent and drug-specific changes in ERK signaling, we used partial correlation analysis to determine pairwise correlations between p-ERK and AP-1 levels across 18 drug-treated cell lines. This analysis identified p-FRA1 as a consistent predictor of p-ERK changes following both MAPK inhibitor conditions (Figure 5B). In agreement with population-level correlation analysis, single-cell analysis also revealed a significant covariance between p-ERK and p-FRA1 levels (Figure 5C). Such strong connection between p-FRA1 and p-ERK is consistent with FRA1 serving as a tightly coupled sensor of ERK activity (Gillies et al., 2017). Together, these data reveal that in addition to predicting the differentiation state of melanoma cells at baseline, AP-1 changes following exposure to MAPK inhibitors are strong predictors of the ways that melanoma cells respond to MAPK inhibition.

Perturbation of AP-1 state by siRNA confirms its role in driving differentiation state heterogeneity

We hypothesized that if the AP-1 state drives melanoma differentiation programs, then inducing perturbations in the AP-1 state will shift differentiation states in predictable ways. To test this

hypothesis, we perturbed AP-1 factors in COLO858 melanoma cells by using pools of previously validated siRNAs to deplete four AP-1 proteins cFOS, FRA2, cJUN, and JUND, either individually or in pairwise combinations. COLO858 represents a heterogenous population composed of both melanocytic and undifferentiated cells, thereby allowing us to track changes in the heterogeneity of differentiation state after AP-1 perturbations. Following 96 h of AP-1 gene knockdown in COLO858 cells, we measured (in three replicates) protein levels of differentiation markers MITF, SOX10 and AP-1 factors cFOS, FRA1, FRA2, cJUN, and JUND using 4i (Figures 6A, 6B). As shown above, cFOS, FRA1, FRA2, and cJUN were able to consistently distinguish melanocytic/transitory ($MITF^{High}$/ $SOX10^{High}$) cells from undifferentiated ($MITF^{Low}$/ $SOX10^{Low}$) cells at the levels of gene expression, protein expression, and regulon activity. We thus asked whether siRNA-induced changes in the levels of these AP-1 proteins would be followed by predictable changes in the fractions of melanocytic/transitory or undifferentiated cells as evaluated by single-cell expression of MITF and SOX10 proteins.

Interestingly, siRNA-mediated knockdowns not only reduced the levels of AP-1 proteins targeted by their corresponding siRNAs but also, in some cases, led to changes in the expression of other AP-1 proteins (Figure 6A). For example, FOSL2 knockdown substantially reduced FRA2 levels, but also induced the expression of FRA1 and cJUN, when compared to cells treated with non-targeting (control) siRNA. JUND knockdown reduced JUND levels, but also led to an increase in cFOS and cJUN levels. These observations agree with previous reports (Lopez-Bergami et al., 2010) indicating that the state of AP-1 network is controlled by feedback regulation and interactions among different AP-1 factors. Combinations of siRNAs against pairs of AP-1 genes may help reveal those interactions that are phenotypically consequential. To identify such interactions, we quantified the levels of SOX10 and MITF proteins across all knockdown conditions (Figure 6B, 6C), then computed the percentage of melanocytic/ transitory ($SOX10^{High}$/ $MITF^{High}$) cells and undifferentiated ($SOX10^{Low}$/ $MITF^{Low}$) cells in

each condition (Figure 6D) and examined them along a two-dimensional plot (Figure 6E). We found that knocking down FOSL2 and JUN in combination, but not individually, reduced the percentage of undifferentiated cells most significantly and by approximately 2-fold (P = 0.002) (Figures 6E, 6F). This behavior is consistent with our finding regarding the role of FRA2 and cJUN in regulation of the undifferentiated state. Furthermore, it shows that the co-depletion of FRA2 and cJUN is essential for blocking the undifferentiated cells that otherwise up-regulate cJUN following the knockdown of FOSL2 alone (Figure 6A). On the other hand, knocking down FOS reduced the percentage of melanocytic/ transitory cells (P = 0.03) (Figures 6E, 6G), which is consistent with our finding regarding its role in driving the melanocytic lineage. Furthermore, the combination of FOS and JUND knockdown dramatically enhanced this effect, leading to a reduction of >2-fold in the percentage of melanocytic /transitory cells (P = 0.0001) and an increase of >2-fold in the percentage of undifferentiated cells (P = 0.01) (Figures 6E, 6G, 6H). As discussed above, this observation also could be explained by the induction of cJUN expression (a driver of dedifferentiation) following JUND knockdown.

Together, these results validate the causality of our statistical predictions for the AP-1 state in contributing to differentiation state plasticity in melanoma cells. They show that a tightly regulated balance between JUN and FOS subfamily members determines the baseline differentiation state of a cell. Directed perturbation of this state leads to changes in the composition of differentiation states in a predictable manner.

Discussion

The hyperactivation of MAPK signaling in BRAF-mutant melanomas is linked to their overall sensitivity to MAPK inhibition. The differentiation state heterogeneity, however, leads to variability in

MAPK inhibitor responses both across genetically diverse tumors and among genetically homogeneous populations of cells. Understanding the origins of such heterogeneity is key to identifying effective strategies to overcome fractional responses that undermine the potential of MAPK-targeted therapies. It requires a detailed knowledge of the mechanisms and molecular players that link epigenetic plasticity and transcriptional regulation of differentiation state to therapy-induced changes in MAPK signaling. To begin to fill this gap in our knowledge, we used a multidimensional approach at single-cell resolution to systematically investigate the AP-1 transcription factor contributions to heterogeneity in BRAF-mutant melanomas. We focus on the AP-1 factors because they serve as downstream targets of MAP kinases, and previous work has connected several AP-1 proteins to MAPK inhibitor resistance, differentiation state heterogeneity, and therapy-induced dedifferentiation in melanomas.

Our data showed that a tightly regulated balance between a few key AP-1 family members and their activities strongly predict previously characterized heterogeneities in melanoma differentiation states. Specifically, cFOS and p-cFOS were associated with melanocytic and transitory cells, while FRA1/p-FRA1, FRA2, and cJUN/p-cJUN correlated with less differentiated cell states. The systematic nature of the study across many genetically different melanomas suggests that these associations are a general feature of melanomas and likely not unique to a particular cell line or linked to a certain genetic context. Furthermore, we showed that perturbing the molecular balance of AP-1 factors in melanoma cells by siRNAs that deplete specific AP-1 proteins, either alone or in combination, or by treatments with MAPK inhibitors can induce differentiation state switching and heterogeneity in a controllable manner. Together, these findings provide new insights into AP-1 function, its role in cell state plasticity, and its potential dysregulation in melanoma, while opening new avenues for interrogating the AP-1 behavior in the context of adaptive response to MAPK inhibitors. In theory, gaining the ability to target

certain AP-1 states could force cells to remain in a more drug-sensitive state, thereby increasing the fractional killing of melanoma cells in response to MAPK inhibition.

Future studies may leverage the findings from this study to further elucidate transcriptional mechanisms that contribute to MAPK-targeted therapy escape in melanomas at a single-cell level. Furthermore, uncovering how the information encoded in the MAPK signaling dynamics is transduced through its downstream AP-1 network will be key for explaining the observed variability in tumor cell responses to MAPK inhibitors. For example, AP-1 family members FOS and FOSL1 are early ERK target genes whose regulation by ERK activity constitutes feedforward motifs that enable them to decode the dynamics of ERK signaling (Davies et al., 2020). Differentiation state-specific variations in the baseline expression and activities of these AP-1 genes, as we observed in this study, could introduce variability in the transduction of MAPK signals, generating heterogeneity in cell fate under MAPK perturbations. Future studies that link dynamic fluctuations in ERK activity and other MAP kinases to AP-1 behavior could offer important insights into mechanisms of heterogeneity in drug response and adaptive resistance to MAPK inhibitors.

Consistent with our findings regarding the role of AP-1 state changes in determining the differentiation state plasticity, recent studies have highlighted a key role for AP-1 factors in chromatin organization and enhancer accessibility. AP-1 proteins have been reported to facilitate new cell fate transitions, such as cellular senescence or differentiation, by establishing the enhancer landscape and granting long-term chromatin access to other transcription factors, thereby allowing the timely execution of cell state-specific transcriptional programs (Madrigal and Alasoo, 2018; Martínez-Zamudio et al., 2020; Phanstiel et al., 2017; Vierbuchen et al., 2017). Understanding which AP-1 factors and cofactors work to keep poised enhancers accessible and which function to shift enhancers from a poised to active state could connect transcription to dedifferentiation and genome reorganization following inhibition of

MAPK signaling and its adaptive reactivation. Furthermore, AP-1 proteins like other bZIP proteins must form dimers before they could bind to the AP-1 motif site. For example, while FOS family members bind DNA as obligate heterodimers with members of the JUN family, JUN family members can bind the AP-1 motif site as both homodimers and heterodimers with FOS family members. Future studies, therefore, should also determine the extent to which the combinatorial activity of AP-1 family members is influenced by distinct patterns of dimerization among these transcription factors.

Acknowledgments

We thank Kevin Janes and members of the Fallahi-Sichani laboratory for helpful suggestions and discussion. This work was supported by NIH grant R35-GM133404 (to MFS), the Farrow Fellowship (to DB) and P30-CA044579 (University of Virginia Cancer Center Support Grant). We acknowledge Research Computing at The University of Virginia for providing computational resources and technical support.

Author Contributions

N.C.-L., D.G.B. and M.F.-S. conceived and designed the study and wrote the manuscript; N.C.-L. performed computational model analysis. D.G.B. developed protocols and performed the experiments. N.C.-L. and D.G.B. performed experimental data analysis. M.F.-S. supervised the work.

Declaration of interests

The authors declare that they have no competing interests directly or indirectly related to the content of this manuscript.

Materials and Methods

Cell culture and drug treatments

BRAF-mutant melanoma cell lines used in this study were obtained from the following sources: COLO858 (from ECACC), RVH421 (from DSMZ), A375, A375(NRAS^{Q61K}), C32, A2058, WM115, SKMEL28, HS294T, WM1552C, SKMEL5, A101D, and IGR39 (all from ATCC), LOXIMV1 (from DCTD Tumor Repository, National Cancer Institute), MMACSF (RIKEN BioResource Center), WM902B and WM2664 (from Wistar Institute), UACC62 and SKMEL19 (from the Cancer Cell Line Encyclopedia). All cell lines have been subjected to re-confirmation by short tandem repeat (STR) profiling by ATCC and mycoplasma testing by MycoAlert™ PLUS Mycoplasma Detection Kit (Lonza). A375, A375(NRAS^{Q61K}), A2058, HS294T, A101D, and IGR39 cells were grown in DMEM with 4.5 g/l glucose (Corning, Cat# 10-013-CV) supplemented with 5% fetal bovine serum (FBS) (Gibco Cat. No. 26140079). SKMEL5 and WM2664 cells were grown in EMEM (Corning, Cat# 10-009-CV) supplemented with 5% FBS. C32, MMACSF, SKMEL28, and WM115 cells were grown in DMEM/F12 (Gibco, Cat# 11330-032) supplemented with 1% sodium pyruvate (Gibco Cat. No. 11360070) and 5% FBS. COLO858, LOXIMVI, RVH421, SKMEL19, UACC62, WM1552C, and WM902B cells were grown in RPMI 1640 (Corning, Cat# 10-040-CV) supplemented with 1% sodium pyruvate and 5% FBS. Cells were grown at 37°C with 5% CO_2 in a humidified chamber. 100 U/mL Penicillin-Streptomycin (10,000 U/mL), and 0.5 mg/mL Plasmocin Prophylactic (Invivogen Cat. No. NC9886956) were present in all cell cultures. Cells were seeded in 200 µl/well in Corning 96-well plates (Cat. No. 3904).

Vemurafenib (Selleck Chemicals Cat. No. S1267), Trametinib (Selleck Chemicals Cat. No. S2673) or vehicle (DMSO) was added at indicated concentrations using the Tecan D300e Digital Dispenser 24 hours after cell seeding. Cells were fixed at the indicated timepoints with 4% paraformaldehyde in phosphate-buffered saline (PBS) for 30 minutes at room temperature.

AP-1 gene knockdown by siRNA

COLO858 cells were seeded in 100 µl of antibiotic-free growth media (RPMI supplemented with 5% FBS and 1 mM Sodium Pyruvate) in 96-well plates at a density of 2000 cells/well. After 24 h of incubation, cells were transfected using 0.05 µl of DharmaFECT 2 reagent (Horizon Discovery Cat. No. T-2002-01) per well with indicated Dharmacon ON-TARGETplus AP-1 siRNAs (at 25 nM) individually or in pairwise combinations. Knockdowns targeting a single AP-1 gene were supplemented with non-targeting siRNA to normalize the final siRNA concentration (to 50 nM siRNA) across all siRNA conditions. All siRNAs were tested for knockdown efficiency and specificity by measuring protein levels of each factor and members of the factor subfamily (i.e., measure single-cell protein levels of cFOS, FRA1, and FRA2 following FOS knockdown). Only siRNA species that showed knockdown of the protein target without off-target knockdown effects were used. Cells were fixed 96 hours after transfection with 4% paraformaldehyde in PBS for 30 minutes at room temperature. The siRNA sequences used for each condition are included below:

Target Gene	**Dharmacon Cat#**	**siRNA sequence**
Non-targeting control	D-001810-10-05	UGGUUUACAUGUCGACUAA, UGGUUUACAUGUUGUGUGA, UGGUUUACAUGUUUUCUGA, UGGUUUACAUGUUUUCCUA

FOS	J-003265-09	GGGAUAGCCUCUCUUACUA
	J-003265-10	ACAGUUAUCUCCAGAAGAA
	J-003265-12	GCAAUGAGCCUUCCUCUGA
FOSL1	J-004341-06	GAGCUGCAGUGGAUGGUAC
	J-004341-07	AAUCUGGGCUGCAGCGAGA
	J-004341-08	GAGUAAGGCGCGAGCGGAA
FOSL2	J-004110-13	GGCCCAGUGUGCAAGAUUA
cJUN	J-003268-10	GAGCGGACCUUAUGGCUAC
	J-003268-12	GAAACGACCUUCUAUGACG
JUND	J-003900-12	GAAACACCCUUCUACGGCG
	J-003900-13	CCGACGAGCUCACAGUUCC
	J-003900-14	UCAAGAGUCAGAACACGGA
	J-003900-15	GUUCGAUUCUGCCCUAUUU

Iterative indirect immunofluorescence imaging (4i)

4i images were obtained using the protocol described by Gut et. al. (Gut et al., 2018) with minor modifications. After media aspiration, cells in 96-well plates were fixed with 4% paraformaldehyde in PBS for 30 minutes at room temperature. All washes were performed using a BioTek EL406 Washer Dispenser and consisted of 4 wash cycles of 200 µl with the indicated buffer while retaining approximately 20 µl liquid in each well during the aspiration step to limit cell loss. Cells were washed with PBS then permeabilized for 15 minutes at room temperature with 100 µl 0.5% Triton X-100 in PBS. Cells were washed with PBS followed by Milli-Q deionized water. Cells were next treated 3 times total for 12 minutes each instance with 40 µl elution buffer which consists of 0.5M L-Glycine (Sigma-Aldrich Cat. No. 50046), 3M Urea (Sigma-Aldrich Cat. No. U5128), 3 M Guanidinium chloride (Sigma-Aldrich Cat. No. G3272), and 70 mM TCEP-HCl (Sigma-Aldrich Cat. No. C4706) at pH of 2.5. Cells were washed with PBS as above. Samples were then blocked for 1 h at room temperature with 50 µl

blocking buffer which consists of PBS-based Intercept buffer (LiCor Cat. No. 927-70001) supplemented with 150 mM maleimide (Millipore Sigma Cat. No. 129585-25G). Blocking buffer was prepared immediately prior to adding to the samples for each round. Following a PBS wash, samples were incubated overnight at 4°C with 40 µl primary antibody diluted in Intercept buffer. After overnight incubation, cells were washed with PBS then incubated for 1 hour at room temperature in 40 µl secondary antibody solution consisting of the appropriate species-specific Alexa Fluor-conjugated antibodies diluted 1:2000 in Intercept buffer. Cells were then washed with PBS and incubated with 50 µl Hoechst 33342 (Invitrogen Cat. No. H3570) diluted 1:20,000 in PBS. For the first round of imaging, cells were stained with a mixture of Hoechst and CellMask Green (ThermoFisher Cat. No. C37608) for 30 minutes at room temperature according to the manufacturer's instructions. Next, cells were washed with Milli-Q water and 80 µl imaging buffer consisting of 700 mM N-Acetyl-Cysteine (Sigma-Aldrich Cat. No. A7250) at pH of 7.4. Images were obtained using Operetta CLS high content imaging system (Perkin Elmer) using a 10x air objective lens. Following imaging, samples were washed with Milli-Q water after which antibodies were eluted with 3 successive 12-minute incubations at room temperature with elution buffer. Cells were washed with PBS followed by Milli-Q water. Next, 50 µl imaging buffer was added to each well and samples were imaged as above to assess removal of fluorescent signal. Cells were then washed with PBS and all steps were repeated starting at the blocking step for each round of 4i. In instances where the time between 4i rounds exceeded 3 days, following elution, the plates were fixed for 10 minutes at room temperature with 4% paraformaldehyde in PBS. In these cases, to resume staining, cells were then washed with PBS followed by Milli-Q water and treated with elution buffer lacking TCEP-HCl three times for 10 minutes, totaling 30 minutes. Afterwards, cells were washed with PBS and the next round of 4i commenced. The following primary antibodies were used in immunostaining assays.

Target	Antibody Name	Manufacturer	Cat#
c-FOS	c-Fos (9F6) Rabbit mAb	Cell Signaling Technologies	2250
p-c-FOS	Phospho-c-Fos (Ser32) (D82C12) XP® Rabbit mAb	Cell Signaling Technologies	5348
FRA1	Recombinant Anti-FRA1 [EP4711] Rabbit mAb	Abcam	ab124722
p-FRA1	Phospho-FRA1 (Ser265) (D22B1) Rabbit mAb	Cell Signaling Technologies	5841
FRA2	Fra2 (D2F1E) Rabbit mAb	Cell Signaling Technologies	19967
cJUN	c-Jun (60A8) Rabbit mAb	Cell Signaling Technologies	9165
p-cJUN	Phospho-c-Jun (Ser73) (D47G9) XP® Rabbit mAb	Cell Signaling Technologies	3270
JUND	JunD (D17G2) Rabbit mAb	Cell Signaling Technologies	5000
JUNB	JunB (C37F9) Rabbit mAb	Cell Signaling Technologies	3753
p-ATF1	Phospho Anti-ATF1 (S63) Rabbit mAb	Abcam	ab76085
ATF2	Recombinant Anti-ATF2 [E243]	Abcam	ab32160
p-ATF2	Recombinant Anti-ATF2 (phospho T71) [E268]	Abcam	ab32019
ATF3	Anti ATF3	Abcam	ab87213
ATF4	Recombinant Anti-ATF4 antibody [EPR18111]	Abcam	ab184909
p-ATF4	Anti-ATF4 (phospho S245)	Abcam	ab28830
ATF5	Recombinant Anti-ATF5 [EPR18286]	Abcam	ab184923
ATF6	Anti-ATF6 antibody [1-7]	Abcam	ab122897
p-ERK	Phospho pErk1/2 (T202/Y204) Rabbit mAb	Cell Signaling Technologies	4370
MITF	Human MITF Antibody	R&D Systems	AF5769
SOX10	Anti-SOX10 antibody [SOX10/991]	Abcam	ab212843
NGFR	p75NTR Rabbit mAb	Cell Signaling Technologies	8238
AXL	Human Axl Antibody	R&D Systems	AF154

Image analysis

Images were background subtracted using the rolling ball subtraction algorithm in ImageJ. Background-subtracted images from each round of 4i were aligned using Hoechst nuclei staining with CellProfiler 3.1.9 using the normalized cross correlation method within the Align module. Nuclei were segmented from the aligned images using the Minimum Cross Entropy thresholding method within the

IdentifyPrimaryObjects module in CellProfiler. The Threshold smoothing scale and correction factor were 2.4 and 1, respectively with lower and upper threshold bounds of 0 and 1. Cell segmentation was then performed using CellMask Green staining to propagate objects from the nuclei. This was done using the Propagation method within the IdentifySecondaryObjects module. The Minimum cross entropy thresholding method was employed with a smoothing scale of 0 and correction factor of 1, the lower and upper threshold bound values set to 0 and 1, and a regularization factor of 0.05. The TrackObjects module was used to multiplex data from individual rounds of 4i. Within TrackObjects, the Follow Neighbors method was used with the maximum pixel distance of 50 and average cell diameter of 15. Comma-separated text files containing quantitative single-cell measurements of tracked objects from CellProfiler were organized using Matlab. Only objects present in every round of imaging were included in the analysis. Additional data analysis was performed using Matlab, R, and Python.

Classifying melanoma differentiation states

To classify the differentiation state of cells based on image-based protein measurements, we generated histograms of single-cell data on each of the previously validated melanoma differentiation state markers (MITF, SOX10, NGFR and AXL) (Khaliq et al., 2021; Tsoi et al., 2018). For each protein (X), we identified an appropriate binary gate, based on which individual melanoma cells were divided into two groups of X^{High} and X^{Low} cells. The gating thresholds used on background-subtracted image data for each protein included: log(MITF) = 7.37, log(SOX10) = 6.82, log(NGFR) = 4.61, and log(AXL) = 5.60. We then used these classifications to determine the differentiation subtype of each individual melanoma cell as follows: melanocytic (M): $MITF^{High}$ /$SOX10^{High}$ /$NGFR^{Low}$ /AXL^{Low}; transitory (T): $MITF^{High}$ /$SOX10^{High}$ /$NGFR^{High}$ /AXL^{Low}; neural crest-like (N): $MITF^{Low}$ /$SOX10^{High}$ /$NGFR^{High}$ /AXL^{High}; and undifferentiated (U): $MITF^{Low}$ /$SOX10^{Low}$ /$NGFR^{Low}$ /AXL^{High}; the single-cell analysis and baseline

differentiation state classification were performed across 19 different melanoma cell lines representing a wide spectrum of differentiation states. To classify the differentiation state of cells in gene knockdown perturbation assays, we used a similar approach to distinguish melanocytic/transitory ($MITF^{High}$ /$SOX10^{High}$) cells from undifferentiated ($MITF^{Low}$ /$SOX10^{Low}$) cells.

To classify melanoma differentiation states using bulk transcriptomic data, each melanoma cell line was assigned a series of seven differentiation signature scores, defined as the average of z-scores for the expression levels of differentiation state signature genes identified previously by Tsoi *et al* (Tsoi et al., 2018). These differentiation signatures included the four main differentiation signatures, i.e., melanocytic (M), transitory (T), neural crest-like (N) and undifferentiated (U), as well as mixtures of neighboring signatures, including melanocytic-transitory (MT), transitory-neural crest-like (TN) and neural crest-like-undifferentiated states (NU).

To determine the differentiation state of individual cells for each of the 10 melanoma cell lines profiled by single-cell RNA sequencing by Wouters *et al* (Wouters et al., 2020), we used the R package AUCell to quantify the enrichment of differentiation signature genes (as defined by Tsoi *et al* (Tsoi et al., 2018)) in individual cells. Because not all differentiation states were equally represented by the 10 cell lines tested and not all signature genes were available in the expression matrix, we focused our single-cell differentiation state classification on melanocytic, transitory and undifferentiated states by combining two or three closely related signature gene sets as follows: M-MT gene set (combination of M and MT signature genes), MT-T-TN gene set (combination of MT, T and TN signature genes) and NU-U set (combination of NU and U genes). To minimize the impact of noise from single-cell analysis, we then selected cells that represented individual differentiation states based on their gated AUCell scores as follows: melanocytic cells: $M\text{-}MT^{High}/NU\text{-}U^{Low}$; transitory cells: $MT\text{-}T\text{-}TN^{High}/NU\text{-}U^{Low}$; undifferentiated cells: $M\text{-}MT^{Low}$/ $MT\text{-}T\text{-}TN^{Low}/NU\text{-}U^{High}$. The differentiation state of individual

melanoma cells derived from treatment-naïve patient tumors profiled by Tirosh *et al* (Tirosh et al., 2016) and Jerby-Arnon *et al* (Jerby-Arnon et al., 2018) were determined in the same way, except that only melanocytic and undifferentiated cells were identified and analyzed.

Random forest classification

We used random forest classification to test the predictivity of AP-1 variations for melanoma differentiation state using single-cell protein data collected by immunofluorescence imaging of 19 melanoma cell lines. We randomly sampled a total of 10,000 cells, including 2,500 from each of the four differentiation states, in a way that they represented all 19 cell lines and 4 distinctive differentiation states (melanocytic, transitory, neural crest-like and undifferentiated) as equally as possible. By random sampling, we aimed to minimize potential biases associated with genotype differences among cell lines. We used the data from 80% of the sampled cells to train a random forest classification model to predict the differentiation state of each individual cell. We then used the remaining 20% of cells to independently validate model predictions. Model training, cross-validation and independent validation were all performed in Python (3.9.2) using the scikit-learn library (0.24.1) (Pedregosa et al.). To standardize the model input, protein levels of each AP-1 measurement were normalized across cells to zero mean and unit variance (z-score scaled) using the StandardScaler() function. The random forest model was trained using the RandomForestClassifier() function. All parameters were as defined in the default settings, except the number of trees in the forest (n_estimators = 100) and maximum tree depth (max_depth = 14), which were separately optimized through 5-fold Stratified Shuffle Split cross-validation on the training set, using the StratifiedShuffleSplit() function with 10 times splitting iterations (n_splits = 10).

The random forest model performance was evaluated based on accuracy and Area Under the Receiver Operating Characteristic Curve (ROC AUC). Accuracy reports the fraction of correctly classified samples, i.e., true positives and true negatives, and it was calculated using the accuracy_score() function. The ROC AUC scores were calculated using the roc_auc_score() function with the One-vs-rest option (multi_class = 'ovr'), which computes the AUC of each class against the rest. The ROC AUC scores consider both the sensitivity (true positive rate) and specificity (true negative rate) of the model predictions.

To assess the importance of each AP-1 factor in explaining the predictions made by the random forest model for each individual cell in the independent validation set, we used the SHapley Additive exPlanations (SHAP) package (Lundberg and Lee, 2017). SHAP provides a model agnostic measure of feature importance based on Shapley values, which assign importance of input features based on their contribution to the model output prediction. Mathematically, given a specific prediction output by model *f* with input *x*, Shapley value for feature *i*, $\varphi_i(f,x)$, is the average of feature *i's* marginal contributions across all possible orders of features being included (Lundberg and Lee, 2017; Lundberg et al., 2018):

$$\varphi_i(f,x) = \sum_{S \subseteq S_{all \setminus \{i\}}} \frac{|S|!\,(M-|S|-1)!}{M!} [f_x(S \cup \{i\}) - f_x(S)]$$

where *M* is the total number of features, |*S*| denotes number of entries in set *S* and the term $f_x(S \cup \{i\}) - f_x(S)$ is the marginal contribution of feature *i*. In SHAP, the marginal impact of a feature is defined as the change in the expected value of the model output *f(x)* when that feature is observed versus unknown:

$$f_x(S \cup \{i\}) - f_x(S) = \mathrm{E}\left[f(x) \mid x_{s \cup \{i\}}\right] - \mathrm{E}[f(x) \mid x_s]$$

, where x_s is a subset of features with only set *S* is observed.

Partial least squares regression (PLSR) modeling

We used PLSR analysis to test whether the relationships between the patterns of AP-1 gene expression and melanoma differentiation state were recapitulated at the transcriptional level. Bulk RNA sequencing data of 53 melanoma cell lines used for PLSR analysis were deposited by Tsoi *et al* (Tsoi et al., 2018) in the Gene Expression Omnibus (GEO) database under accession number GSE80829. We first $\log_2$-transformed the gene expression data (reported as FPKM) with an offset of 1. Input vectors for PLSR analysis were then created by combining the z-scored expression data for fifteen AP-1 transcription factor family genes, including FOS, FOSL1, FOSL2, FOSB, JUN, JUNB, JUND, ATF1, ATF2, ATF3, ATF4, ATF5, ATF6, ATF6B and ATF7, across 53 cell lines. The response variables for each cell line were then assembled as a series of seven signature scores, defined as the average of z-scores for the expression levels of differentiation state signature genes (Tsoi et al., 2018). The PLSR model was trained in python using the scikit-learn library and the PLSRegression() function. To evaluate the predictability of the linear relationship between the input and output variables using the same dataset, we used leave-one-out cross-validation by LeaveOneOut() function. To independently validate the model, we used RNA sequencing data from an independent panel of 32 melanoma cell lines in the Cancer Cell Line Encyclopedia (CCLE) (Ghandi et al., 2019). The CCLE data (CCLE_RNAseq_genes_rpkm_20180929.gct data) was downloaded from https://sites.broadinstitute.org/ccle. As with the training dataset, we first $\log_2$-transformed the CCLE gene expression data (reported as RPKM) with an offset of 1. We then created input vectors by combining the z-scored expression data for fifteen AP-1 transcription factor family genes and used them in the optimized PLSR model (using the first four PLS components) trained against the original set of 53 cell lines to predict the differentiation signature scores in the new set of 32 cell lines.

The PLSR model performance was evaluated in terms of fraction of variance explained (R^2) or predicted (Q^2) using the explained_variance_score() function. We assessed the relative importance of each AP-1 factor in the PLSR model based on the variable importance in projection (VIP) scores, computed for the first four PLS components, at which the PLSR model achieves its optimal performance (Wold, 1994). To help interpret the directionality of the contribution, we multiplied the VIP score for each AP-1 factor by the sign of Pearson correlation coefficient between its expression levels and differentiation signature z-scores.

We compared the performance (based on 10-fold cross validation) of optimized PLSR model, built based on the top eight AP-1 genes (FOS, FOSL1, FOSL2, JUN, JUNB, JUND, ATF2 and ATF4) with optimized models built using combinations of eight randomly chosen basic leucine zipper (bZIP) transcription factors (Vinson et al., 2002) or eight randomly chosen transcription factors (Van de Sande et al., 2020) (excluding those that were explicitly involved in the differentiation signature genes) by computing empirical *P* values using 100,000 and 500,000 iterations, respectively.

Uniform manifold approximation and projection (UMAP)

UMAP was performed in R using the umap package. For single-cell protein data, we first performed principal component analysis (PCA) using the prcomp() function on the z-scored log-transformed data and selected the PCA scores from the first four principal component for UMAP analysis. The parameters used in generating the UMAP for single-cell protein data include nearest neighbor (n_neighbors) = 90, minimum distance (min_dist) = 0.7 and distance metric (metric) = Euclidean.

Single-cell regulatory network inference and clustering (SCENIC)

For the SCENIC analysis of melanoma cell lines, the baseline regulon activities inferred by the SCENIC workflow (Aibar et al., 2017; Van de Sande et al., 2020) were obtained from the .loom file (10_Baselines_filteredRegulons.loom) published by Wouters *et al* (Wouters et al., 2020) (http://scope.aertslab.org/#/Wouters_Human_Melanoma). The .loom file was imported to R for downstream analysis using the SCopeLoomR package.

Single-cell RNA sequencing data for patient-derived melanoma tumors were obtained from previous studies published by Tirosh *et al* (Tirosh et al., 2016) and Jerby-Arnon *et al* (Jerby-Arnon et al., 2018) (GSE72056 and GSE115978). Single-cell gene expression analysis and SCENIC was focused on 2072 malignant melanoma cells, which were distinguished (by the authors) from non-malignant cells based on gene copy number variations We selected 14,689 genes which were detected in more than 1% of the cells (i.e., 20 cells) with at least 103 logged TPM counts. Using this dataset, we then inferred regulons using pySCENIC in a Nextflow pipeline adapted from Wouters *et al* (Wouters et al., 2020) (https://github.com/aertslab/singlecellRNA_melanoma_paper), performing 100 SCENIC runs on the data. As in Wouters *et al*'s regulon filtering criteria, only regulons that had more than 10 target genes and recurred in at least 80/100 runs were retained. Target genes (used in AUCell calculation) that appear in at least 80% of the runs in regulons that recurred 100 times, and all target genes for regulons that recurred 80-100 times were retained. This analysis pipeline resulted in 373 motif regulons.

Partial correlation analysis

Partial correlation analysis is used for the evaluation of correlations between pairs of variables while controlling for the variance explained by a third variable. We used pairwise partial correlation analysis to evaluate correlations among changes induced by MAPK inhibitors in each of the AP-1 protein levels,

dedifferentiation, and p-ERK levels across different cell lines, while controlling for the baseline (drug-naïve) variance of differentiation state or AP-1 levels across the same cell lines. To identify possible associations between AP-1 factors and drug-induced dedifferentiation, we first calculated the relative enrichment of dedifferentiated cells at each treatment condition (including the baseline) by subtracting the fraction of cells that are $NGFR^{Low}/MITF^{High}$ from the fraction of cells that are $NGFR^{High}/MITF^{Low}$ at that condition. AP-1 data were also averaged across two replicates and log-transformed. We then used the Matlab function partialcorr to evaluate the Pearson's partial correlation coefficients (and the associated *P* values) between the enrichment of dedifferentiated cells and AP-1 data for each MAPK inhibitor treatment condition, while correcting for the variance in the enrichment of dedifferentiated cells at baseline (DMSO condition). Similarly, to assess if any of the AP-1 factors would capture drug-specific changes in ERK signaling, we used partial correlation analysis to determine pairwise correlations between p-ERK and AP-1 levels across drug-treated cell lines, while correcting for differences in their baseline AP-1 levels.

Statistics and reproducibility

No statistical method was used to predetermine sample size. Sample sizes were chosen based on similar studies in the relevant literature. The experiments were not randomized. The investigators were not blinded to allocation during experiments and outcome assessment. All data with error bars were presented as mean values ± s.d. as indicated in figure legends using indicated numbers of replicates. The significance of pairwise correlations were evaluated based on P values associated with the corresponding two-sided Pearson's correlation analysis. To identify the statistical significance of differences between mean of measurements within two different groups *P* values from two-sided *t* test

were used. Statistical analyses were performed using MATLAB (2020b), R (4.0.4), Python (3.9.2), Scikit-learn Library (0.24.1).

Resource Availability

Lead contact

Further information and requests for resources and reagents should be directed to and will be fulfilled by the Lead Contact, Mohammad Fallahi-Sichani (fallahi@virginia.edu).

Materials availability

This study did not generate new unique reagents.

Data and code availability

All unprocessed data generated in this study and the custom scripts used for data analysis are available upon request and will be available on GitHub following publication.

Figure Legends

Figure 1. Single-cell AP-1 protein levels predict differentiation state heterogeneity in melanoma cells. (A) Schematic representation of the iterative indirect immunofluorescence imaging (4i) procedure used in this study to generate multiplexed single-cell data on 17 AP-1 proteins and 4 differentiation state

markers. Representative images of selected AP-1 transcription factors and differentiation state markers are shown for LOXIMVI cells. Scale bars represent 20 µm. Hoechst staining of nuclei is shown in blue while staining of the indicated protein is shown in red. **(B)** Population-averaged measurements of 17 AP-1 proteins and 4 differentiation state markers acquired across 19 BRAF-mutant melanoma cell lines. Protein data shown for each condition represent the log-transformed mean values for two replicates, followed by z-scoring across all cell lines. **(C)** Single-cell distribution of differentiation state markers MITF, SOX10, NGFR and AXL across 19 cell lines, shown by violin plots highlighting the median and interquartile (25% and 75%) ranges. **(D)** The percentage of cells sampled from each of the 19 cell lines, and their corresponding differentiation states (defined based on MITF, SOX10, NGFR and AXL levels) used in the random forest model. **(E)** Confusion matrix showing the independent validation performance of the random forest classifier in predicting the differentiation state of cells based on single-cell AP-1 measurements. The model was trained using a group of 8,000 cells and validated using an independent group of 2,000 cells. The prediction accuracy and area under the receiver operating characteristic curve (ROC AUC) are shown as an overall measure of the classifier performance. **(F)** Distributions of Shapley Additive exPlanations (SHAP) scores for each AP-1 factor across individual cells from the independent validation set. The color indicates the z-score scaled, log-transformed level of each AP-1 protein at a single-cell level. For each differentiation state, AP-1 factors are ordered based on the mean absolute values of their SHAP scores. **(G)** Classification performance of the random forest model based on varying numbers of top AP-1 factors (based on their SHAP values) used as predictors. **(H)** UMAP analysis of the sampled melanoma cells (as shown in **D**) based on their multiplexed levels of top 6 predictive AP-1 measurements (FRA2, p-cFOS, ATF4, cFOS, p-FRA1 and cJUN) results in a continuous trajectory of differentiation states. **(I)** Single-cell levels of the top six AP-1 proteins overlaid on UMAP plots.

Figure 2. AP-1 transcript levels predict variations in differentiation state across melanoma lines. **(A)** Comparison between differentiation signature scores computed based on RNA sequencing data for 53 cell lines reported by Tsoi *et al* (Tsoi et al., 2018) (left) and PLSR-predicted scores (following leave-one-out cross-validation) for each cell line based on their transcript levels of 15 AP-1 genes (right). M: melanocytic; MT: melanocytic-transitory; T: transitory; TN: transitory-neural crest-like; N: neural crest-like; NU: neural crest-like-undifferentiated; U: undifferentiated. **(B)** Performance of the PLSR model evaluated by computing the fraction of variance in differentiation signature scores explained (R^2) or predicted based on leave-one-out cross validation (Q^2) with increasing number of PLS components. **(C)** Comparison between differentiation signature scores computed based on RNA sequencing data of 32 CCLE cell lines (left) and predicted scores based on the PLSR model built for the original set of 53 cell lines (right). **(D)** PLSR scores (of the first two PLS components) for each cell line colored according to their differentiation signature scores for melanocytic, transitory, neural crest-like and undifferentiated states. **(E)** PLSR-derived variable importance in projection (VIP) scores, highlighting combinations of AP-1 transcripts that are predictive of differentiation signature scores for melanocytic, transitory, neural crest-like and undifferentiated states. The sign of the VIP score shows whether the indicated variable (AP-1 transcript level) positively or negatively contributes to a given differentiation signature. Only significant VIP scores (of greater than 1 or smaller than -1) are highlighted. **(F)** Comparison of performance (with respect to differentiation state prediction) between the PLSR model based on transcript levels of the top 8 AP-1 transcription factors with models based on transcript levels of combinations of 8 randomly chosen bZIP family transcription factors ($n = 1\times10^5$ iterations; left panel) or built based on 8 randomly chosen transcription factors ($n = 5\times10^5$ iterations; right panel). Empirical P values were reported for the comparison of predicted variances based on ten-fold cross-validation.

Figure 3. Single-cell network inference reveals the role of AP-1 activity in regulation of differentiation state programs. (A-D) Single-cell distributions of the activity of SCENIC regulons for FOSL2 **(A)**, JUN **(B)**, FOSL1 **(C)** and FOS **(D)** motifs, measured using AUCell in individual cells (from 10 melanoma cell lines profiled by Wouters *et al* (Wouters et al., 2020)) across distinct differentiation states. The differentiation state of individual cells was determined based on their gated levels of enrichment (quantified by AUCell) for the differentiation gene signatures as defined by Tsoi *et al* (Tsoi et al., 2018). **(E-I)** Single-cell distributions of the AUCell activity of SCENIC regulons for FOSL2 **(E)**, JUN **(F)**, FOSL1 **(G)**, and FOS **(H)** motifs, as well as the ratio of FOS and JUN regulon activities **(I)**, quantified in individual cells from 11 treatment-naïve melanoma tumors as profiled by Tirosh *et al* (Tirosh et al., 2016) and Jerby-Arnon *et al* (Jerby-Arnon et al., 2018). Statistical comparisons were performed using two-sided unpaired *t* test. Boxplot hinges correspond to the lower and upper quartiles, with a band at median. Whiskers indicate 1.5 times interquartile ranges.

Figure 4. MAPK inhibitor-induced changes in cJUN/p-cJUN levels correlate with drug-induced dedifferentiation. (A) Population-averaged measurements of 17 AP-1 proteins, differentiation state markers MITF and NGFR, and p-ERK$^{T202/Y204}$ levels acquired across 18 BRAF-mutant melanoma cell lines. Protein data shown for each condition represent the log-transformed mean values for two replicates, followed by z-scoring across all cell lines and treatment conditions, including DMSO, vemurafenib alone (at 0.316 μM) or the combination of vemurafenib (at 0.316 μM) and trametinib (at 0.0316 μM) for 24 or 72 h. **(B)** Single-cell distributions of differentiation state markers MITF and NGFR in 5 cell lines that show MAPK inhibitor-induced dedifferentiation, shown by violin plots highlighting the median and interquartile (25% and 75%) ranges. **(C)** Pairwise partial correlations

(evaluated across 18 cell lines) between each of the 17 AP-1 measurements and the enrichment of $NGFR^{High}/MITF^{Low}$ cells relative to $NGFR^{Low}/MITF^{High}$ cells following 72 h treatment with MAPK inhibitors, while correcting for the baseline (drug-naïve) differentiation state of cell lines. Vem: vemurafenib alone; Vem+Tram: vemurafenib and trametinib in combination. **(D)** Analysis of covariance between the levels of p-cJUN or c-JUN and the difference between NGFR and MITF protein levels at the single-cell level across indicated treatment conditions.

Figure 5. MAPK inhibitor-induced changes in p-FRA1 levels correlate with adaptive changes in ERK pathway activity. (A) Single-cell distribution of $p\text{-}ERK^{T202/Y204}$ level and its changes across different conditions, including DMSO, vemurafenib alone (at 0.316 μM) or the combination of vemurafenib (at 0.316 μM) and trametinib (at 0.0316 μM) for 24 or 72 h. Violin plots highlight the median and interquartile (25% and 75%) ranges. **(B)** Pairwise partial correlations (evaluated across 18 cell lines) between each of the 17 AP-1 measurements and p-ERK levels following 24 or 72 h of treatment with MAPK inhibitors, while correcting for the corresponding baseline (drug-naïve) AP-1 levels of cell lines. **(C)** Analysis of covariance between p-FRA1 and p-ERK levels across indicated treatment conditions at the single-cell level.

Figure 6. Perturbation of AP-1 state by siRNA confirms its role in driving differentiation state heterogeneity. (A, B) The effect of siRNA-mediated depletion (for 96 h) of AP-1 proteins cFOS, FRA2, cJUN, and JUND, either individually or in pairwise combinations, on protein levels of cFOS, FRA1, FRA2, cJUN, and JUND **(A)** or differentiation state markers MITF and SOX10 **(B)** in COLO858 cells. Protein data shown for each condition represent the log-transformed mean values for three replicates,

followed by z-scoring across all knockdown conditions. **(C)** Analysis of covariance between SOX10 and MITF protein levels across indicated knockdown conditions at the single-cell level. Dashed lines indicate the gating thresholds for each protein. **(D)** Variation of the percentage of $SOX10^{High}/MITF^{High}$ (melanocytic or transitory; M or T) cells and $SOX10^{High}/MITF^{High}$ (undifferentiated; U) cells following each knockdown condition. **(E)** Two-dimensional projection of siRNA conditions in terms of percentages of melanocytic or transitory cells versus undifferentiated cells at 96 h. **(F-H)** Statistical comparison (using two-sided *t* test) between fractions of cells in undifferentiated or melanocytic/transitory states and indicated siRNA knockdown conditions. The central mark on the plots indicates the median across three replicates.

Supplementary Figure Legends

Figure S1. Single-cell distribution of seventeen AP-1 factors measured across 19 cell lines and shown by violin plots highlighting the median and interquartile (25% and 75%) ranges. Related to Figure 1.

Figure S2. Single-cell distribution of AP-1 protein measurements, including cFOS, p-cFOS, FRA1, p-FRA1, FRA2, cJUN, p-cJUN, JUNB, and JUND, measured in 19 cell lines before and following treatment with MAPK inhibitors for 24 and 72 h. Violin plots highlight the median and interquartile (25% and 75%) ranges. Related to Figure 4.

Figure S3. Single-cell distribution of AP-1 protein measurements, including p-ATF1, ATF2, p-ATF2, ATF3, ATF4, p-ATF4, ATF5 and ATF6, measured in 19 cell lines before and following treatment with

MAPK inhibitors for 24 and 72 h. Violin plots highlight the median and interquartile (25% and 75%) ranges. Related to Figure 4.

Figure S4. Single-cell distribution of melanoma differentiation state markers MITF and NGFR, measured in 19 cell lines before and following treatment with MAPK inhibitors for 24 and 72 h. Violin plots highlight the median and interquartile (25% and 75%) ranges. Related to Figure 4.

References

Aibar, S., González-Blas, C.B., Moerman, T., Huynh-Thu, V.A., Imrichova, H., Hulselmans, G., Rambow, F., Marine, J.-C., Geurts, P., Aerts, J., et al. (2017). SCENIC: single-cell regulatory network inference and clustering. Nat. Methods *14*, 1083–1086.

Arias, A.M., and Hayward, P. (2006). Filtering transcriptional noise during development: concepts and mechanisms. Nat. Rev. Genet. *7*, 34–44.

Baron, M., Tagore, M., Hunter, M.V., Kim, I.S., Moncada, R., Yan, Y., Campbell, N.R., White, R.M., and Yanai, I. (2020). The Stress-Like Cancer Cell State Is a Consistent Component of Tumorigenesis. Cell Syst. *11*, 536-546.e7.

Battich, N., Stoeger, T., and Pelkmans, L. (2015). Control of Transcript Variability in Single Mammalian Cells. Cell *163*, 1596–1610.

Becht, E., McInnes, L., Healy, J., Dutertre, C.-A., Kwok, I.W.H., Ng, L.G., Ginhoux, F., and Newell, E.W. (2018). Dimensionality reduction for visualizing single-cell data using UMAP. Nat. Biotechnol.

Belote, R.L., Le, D., Maynard, A., Lang, U.E., Sinclair, A., Lohman, B.K., Planells-Palop, V., Baskin, L., Tward, A.D., Darmanis, S., et al. (2021). Human melanocyte development and melanoma dedifferentiation at single-cell resolution. Nat. Cell Biol. *23*, 1035–1047.

Boumahdi, S., and de Sauvage, F.J. (2020). The great escape: tumour cell plasticity in resistance to targeted therapy. Nat. Rev. Drug Discov. *19*, 39–56.

Davies, A.E., Pargett, M., Siebert, S., Gillies, T.E., Choi, Y., Tobin, S.J., Ram, A.R., Murthy, V., Juliano, C., Quon, G., et al. (2020). Systems-Level Properties of EGFR-RAS-ERK Signaling Amplify Local Signals to Generate Dynamic Gene Expression Heterogeneity. Cell Syst. *11*, 161-175.e5.

Emert, B.L., Cote, C.J., Torre, E.A., Dardani, I.P., Jiang, C.L., Jain, N., Shaffer, S.M., and Raj, A. (2021). Variability within rare cell states enables multiple paths toward drug resistance. Nat. Biotechnol. *39*, 865–876.

Emmons, M.F., Faião-Flores, F., Sharma, R., Thapa, R., Messina, J.L., Becker, J.C., Schadendorf, D., Seto, E., Sondak, V.K., Koomen, J.M., et al. (2019). HDAC8 Regulates a Stress Response Pathway in Melanoma to Mediate Escape from BRAF Inhibitor Therapy. Cancer Res. *79*, 2947–2961.

Fallahi-Sichani, M., Moerke, N.J., Niepel, M., Zhang, T., Gray, N.S., and Sorger, P.K. (2015). Systematic analysis of BRAFV600E melanomas reveals a role for JNK/c-Jun pathway in adaptive resistance to drug-induced apoptosis. Mol. Syst. Biol. *11*, 797–797.

Fallahi□Sichani, M., Becker, V., Izar, B., Baker, G.J., Lin, J., Boswell, S.A., Shah, P., Rotem, A., Garraway, L.A., and Sorger, P.K. (2017). Adaptive resistance of melanoma cells to RAF inhibition via reversible induction of a slowly dividing de□differentiated state. Mol. Syst. Biol. *13*, 905.

Gerosa, L., Chidley, C., Fröhlich, F., Sanchez, G., Lim, S.K., Muhlich, J., Chen, J.-Y., Vallabhaneni, S., Baker, G.J., Schapiro, D., et al. (2020). Receptor-Driven ERK Pulses Reconfigure MAPK Signaling and Enable Persistence of Drug-Adapted BRAF-Mutant Melanoma Cells. Cell Syst. *11*, 478-494.e9.

Ghandi, M., Huang, F.W., Jané-Valbuena, J., Kryukov, G.V., Lo, C.C., McDonald, E.R., Barretina, J., Gelfand, E.T., Bielski, C.M., Li, H., et al. (2019). Next-generation characterization of the Cancer Cell Line Encyclopedia. Nature *569*, 503–508.

Gillies, T.E., Pargett, M., Minguet, M., Davies, A.E., and Albeck, J.G. (2017). Linear Integration of ERK Activity Predominates over Persistence Detection in Fra-1 Regulation. Cell Syst. *5*, 549-563.e5.

Gupta, P.B., Fillmore, C.M., Jiang, G., Shapira, S.D., Tao, K., Kuperwasser, C., and Lander, E.S. (2011). Stochastic state transitions give rise to phenotypic equilibrium in populations of cancer cells. Cell *146*, 633–644.

Gut, G., Herrmann, M.D., and Pelkmans, L. (2018). Multiplexed protein maps link subcellular organization to cellular states. Science *361*, eaar7042.

Haas, L., Elewaut, A., Gerard, C.L., Umkehrer, C., Leiendecker, L., Pedersen, M., Krecioch, I., Hoffmann, D., Novatchkova, M., Kuttke, M., et al. (2021). Acquired resistance to anti-MAPK targeted therapy confers an immune-evasive tumor microenvironment and cross-resistance to immunotherapy in melanoma. Nat. Cancer *2*, 693–708.

Huang, S. (2009). Non-genetic heterogeneity of cells in development: More than just noise. Development *136*, 3853–3862.

Jerby-Arnon, L., Shah, P., Cuoco, M.S., Rodman, C., Su, M.-J., Melms, J.C., Leeson, R., Kanodia, A., Mei, S., Lin, J.-R., et al. (2018). A Cancer Cell Program Promotes T Cell Exclusion and Resistance to Checkpoint Blockade. Cell *175*, 984-997.e24.

Johannessen, C.M., Johnson, L.A., Piccioni, F., Townes, A., Frederick, D.T., Donahue, M.K., Narayan, R., Flaherty, K.T., Wargo, J.A., Root, D.E., et al. (2013). A melanocyte lineage program confers resistance to MAP kinase pathway inhibition. Nature *504*, 138–142.

Karin, M. (1995). The Regulation of AP-1 Activity by Mitogen-activated Protein Kinases *. J. Biol. Chem. *270*, 16483–16486.

Khaliq, M., Manikkam, M., Martinez, E.D., and Fallahi-Sichani, M. (2021). Epigenetic modulation reveals differentiation state specificity of oncogene addiction. Nat. Commun. *12*, 1536.

Kong, X., Kuilman, T., Shahrabi, A., Boshuizen, J., Kemper, K., Song, J.-Y., Niessen, H.W.M., Rozeman, E.A., Geukes Foppen, M.H., Blank, C.U., et al. (2017). Cancer drug addiction is relayed by an ERK2-dependent phenotype switch. Nature *550*, 270–274.

Konieczkowski, D.J., Johannessen, C.M., Abudayyeh, O., Kim, J.W., Cooper, Z.A., Piris, A., Frederick, D.T., Barzily-Rokni, M., Straussman, R., Haq, R., et al. (2014). A Melanoma Cell State Distinction Influences Sensitivity to MAPK Pathway Inhibitors. Cancer Discov. *4*, 816–827.

Lin, J.Y., and Fisher, D.E. (2007). Melanocyte biology and skin pigmentation. Nature *445*, 843–850.

Lito, P., Pratilas, C.A., Joseph, E.W., Tadi, M., Halilovic, E., Zubrowski, M., Huang, A., Wong, W.L., Callahan, M.K., Merghoub, T., et al. (2012). Relief of profound feedback inhibition of mitogenic signaling by RAF inhibitors attenuates their activity in BRAFV600E melanomas. Cancer Cell *22*, 668–682.

Lopez-Bergami, P., Lau, E., and Ronai, Z. (2010). Emerging roles of ATF2 and the dynamic AP1 network in cancer. Nat. Rev. Cancer *10*, 65–76.

Lundberg, S.M., and Lee, S.-I. (2017). A Unified Approach to Interpreting Model Predictions. In Advances in Neural Information Processing Systems, (Curran Associates, Inc.), p.

Lundberg, S.M., Nair, B., Vavilala, M.S., Horibe, M., Eisses, M.J., Adams, T., Liston, D.E., Low, D.K.-W., Newman, S.-F., Kim, J., et al. (2018). Explainable machine-learning predictions for the prevention of hypoxaemia during surgery. Nat. Biomed. Eng. *2*, 749–760.

Lundberg, S.M., Erion, G., Chen, H., DeGrave, A., Prutkin, J.M., Nair, B., Katz, R., Himmelfarb, J., Bansal, N., and Lee, S.-I. (2020). From local explanations to global understanding with explainable AI for trees. Nat. Mach. Intell. *2*, 56–67.

Madrigal, P., and Alasoo, K. (2018). AP-1 Takes Centre Stage in Enhancer Chromatin Dynamics. Trends Cell Biol. *28*, 509–511.

Marin-Bejar, O., Rogiers, A., Dewaele, M., Femel, J., Karras, P., Pozniak, J., Bervoets, G., Van Raemdonck, N., Pedri, D., Swings, T., et al. (2021). Evolutionary predictability of genetic versus nongenetic resistance to anticancer drugs in melanoma. Cancer Cell *39*, 1135-1149.e8.

Martínez-Zamudio, R.I., Roux, P.-F., de Freitas, J.A.N.L.F., Robinson, L., Doré, G., Sun, B., Belenki, D., Milanovic, M., Herbig, U., Schmitt, C.A., et al. (2020). AP-1 imprints a reversible transcriptional programme of senescent cells. Nat. Cell Biol. *22*, 842–855.

Maurus, K., Hufnagel, A., Geiger, F., Graf, S., Berking, C., Heinemann, A., Paschen, A., Kneitz, S., Stigloher, C., Geissinger, E., et al. (2017). The AP-1 transcription factor FOSL1 causes melanocyte reprogramming and transformation. Oncogene *36*, 5110–5121.

Mica, Y., Lee, G., Chambers, S.M., Tomishima, M.J., and Studer, L. (2013). Modeling neural crest induction, melanocyte specification, and disease-related pigmentation defects in hESCs and patient-specific iPSCs. Cell Rep. *3*, 1140–1152.

Mitchell, S., and Hoffmann, A. (2018). Identifying Noise Sources governing cell-to-cell variability. Curr. Opin. Syst. Biol. *8*, 39–45.

Müller, J., Krijgsman, O., Tsoi, J., Robert, L., Hugo, W., Song, C., Kong, X., Possik, P.A., Cornelissen-Steijger, P.D.M., Foppen, M.H.G., et al. (2014). Low MITF/AXL ratio predicts early resistance to multiple targeted drugs in melanoma. Nat. Commun. *5*, 5712.

Munsky, B., Neuert, G., and van Oudenaarden, A. (2012). Using gene expression noise to understand gene regulation. Science *336*, 183–187.

Pedraza, J.M., and van Oudenaarden, A. (2005). Noise Propagation in Gene Networks. Science *307*, 1965–1969.

Pedregosa, F., Varoquaux, G., Gramfort, A., Michel, V., Thirion, B., Grisel, O., Blondel, M., Prettenhofer, P., Weiss, R., Dubourg, V., et al. Scikit-learn: Machine Learning in Python. Mach. Learn. PYTHON 6.

Phanstiel, D.H., Van Bortle, K., Spacek, D., Hess, G.T., Shamim, M.S., Machol, I., Love, M.I., Aiden, E.L., Bassik, M.C., and Snyder, M.P. (2017). Static and Dynamic DNA Loops form AP-1-Bound Activation Hubs during Macrophage Development. Mol. Cell *67*, 1037-1048.e6.

Rambow, F., Rogiers, A., Marin-Bejar, O., Aibar, S., Femel, J., Dewaele, M., Karras, P., Brown, D., Chang, Y.H., Debiec-Rychter, M., et al. (2018). Toward Minimal Residual Disease-Directed Therapy in Melanoma. Cell *174*, 843-855.e19.

Ramsdale, R., Jorissen, R.N., Li, F.Z., Al-Obaidi, S., Ward, T., Sheppard, K.E., Bukczynska, P.E., Young, R.J., Boyle, S.E., Shackleton, M., et al. (2015). The transcription cofactor c-JUN mediates phenotype switching and BRAF inhibitor resistance in melanoma. Sci. Signal. *8*, ra82.

Riesenberg, S., Groetchen, A., Siddaway, R., Bald, T., Reinhardt, J., Smorra, D., Kohlmeyer, J., Renn, M., Phung, B., Aymans, P., et al. (2015). MITF and c-Jun antagonism interconnects melanoma dedifferentiation with pro-inflammatory cytokine responsiveness and myeloid cell recruitment. Nat. Commun. *6*, 8755.

Rodríguez-Martínez, J.A., Reinke, A.W., Bhimsaria, D., Keating, A.E., and Ansari, A.Z. (2017). Combinatorial bZIP dimers display complex DNA-binding specificity landscapes. ELife *6*.

Shaffer, S.M., Dunagin, M.C., Torborg, S.R., Torre, E.A., Emert, B., Krepler, C., Beqiri, M., Sproesser, K., Brafford, P.A., Xiao, M., et al. (2017). Rare cell variability and drug-induced reprogramming as a mode of cancer drug resistance. Nature *546*, 431–435.

Sharma, S.V., Lee, D.Y., Li, B., Quinlan, M.P., Takahashi, F., Maheswaran, S., McDermott, U., Azizian, N., Zou, L., Fischbach, M.A., et al. (2010). A chromatin-mediated reversible drug-tolerant state in cancer cell subpopulations. Cell *141*, 69–80.

Symmons, O., and Raj, A. (2016). What's Luck Got to Do with It: Single Cells, Multiple Fates, and Biological Nondeterminism. Mol. Cell *62*, 788–802.

Tirosh, I., Izar, B., Prakadan, S.M., Wadsworth, M.H., Treacy, D., Trombetta, J.J., Rotem, A., Rodman, C., Lian, C., Murphy, G., et al. (2016). Dissecting the multicellular ecosystem of metastatic melanoma by single-cell RNA-seq. Science *352*, 189–196.

Torre, E.A., Arai, E., Bayatpour, S., Jiang, C.L., Beck, L.E., Emert, B.L., Shaffer, S.M., Mellis, I.A., Fane, M.E., Alicea, G.M., et al. (2021). Genetic screening for single-cell variability modulators driving therapy resistance. Nat. Genet. *53*, 76–85.

Tsoi, J., Robert, L., Paraiso, K., Galvan, C., Sheu, K.M., Lay, J., Wong, D.J.L., Atefi, M., Shirazi, R., Wang, X., et al. (2018). Multi-stage Differentiation Defines Melanoma Subtypes with Differential Vulnerability to Drug-Induced Iron-Dependent Oxidative Stress. Cancer Cell *33*, 890-904.e5.

Van de Sande, B., Flerin, C., Davie, K., De Waegeneer, M., Hulselmans, G., Aibar, S., Seurinck, R., Saelens, W., Cannoodt, R., Rouchon, Q., et al. (2020). A scalable SCENIC workflow for single-cell gene regulatory network analysis. Nat. Protoc. *15*, 2247–2276.

Vierbuchen, T., Ling, E., Cowley, C.J., Couch, C.H., Wang, X., Harmin, D.A., Roberts, C.W.M., and Greenberg, M.E. (2017). AP-1 Transcription Factors and the BAF Complex Mediate Signal-Dependent Enhancer Selection. Mol. Cell *68*, 1067-1082.e12.

Vinson, C., Myakishev, M., Acharya, A., Mir, A.A., Moll, J.R., and Bonovich, M. (2002). Classification of Human B-ZIP Proteins Based on Dimerization Properties. Mol. Cell. Biol. *22*, 6321–6335.

Wold, S. (1994). Exponentially weighted moving principal components analysis and projections to latent structures. Chemom. Intell. Lab. Syst. *23*, 149–161.

Wouters, J., Kalender-Atak, Z., Minnoye, L., Spanier, K.I., De Waegeneer, M., Bravo González-Blas, C., Mauduit, D., Davie, K., Hulselmans, G., Najem, A., et al. (2020). Robust gene expression programs underlie recurrent cell states and phenotype switching in melanoma. Nat. Cell Biol. *22*, 986–998.

Figure 1

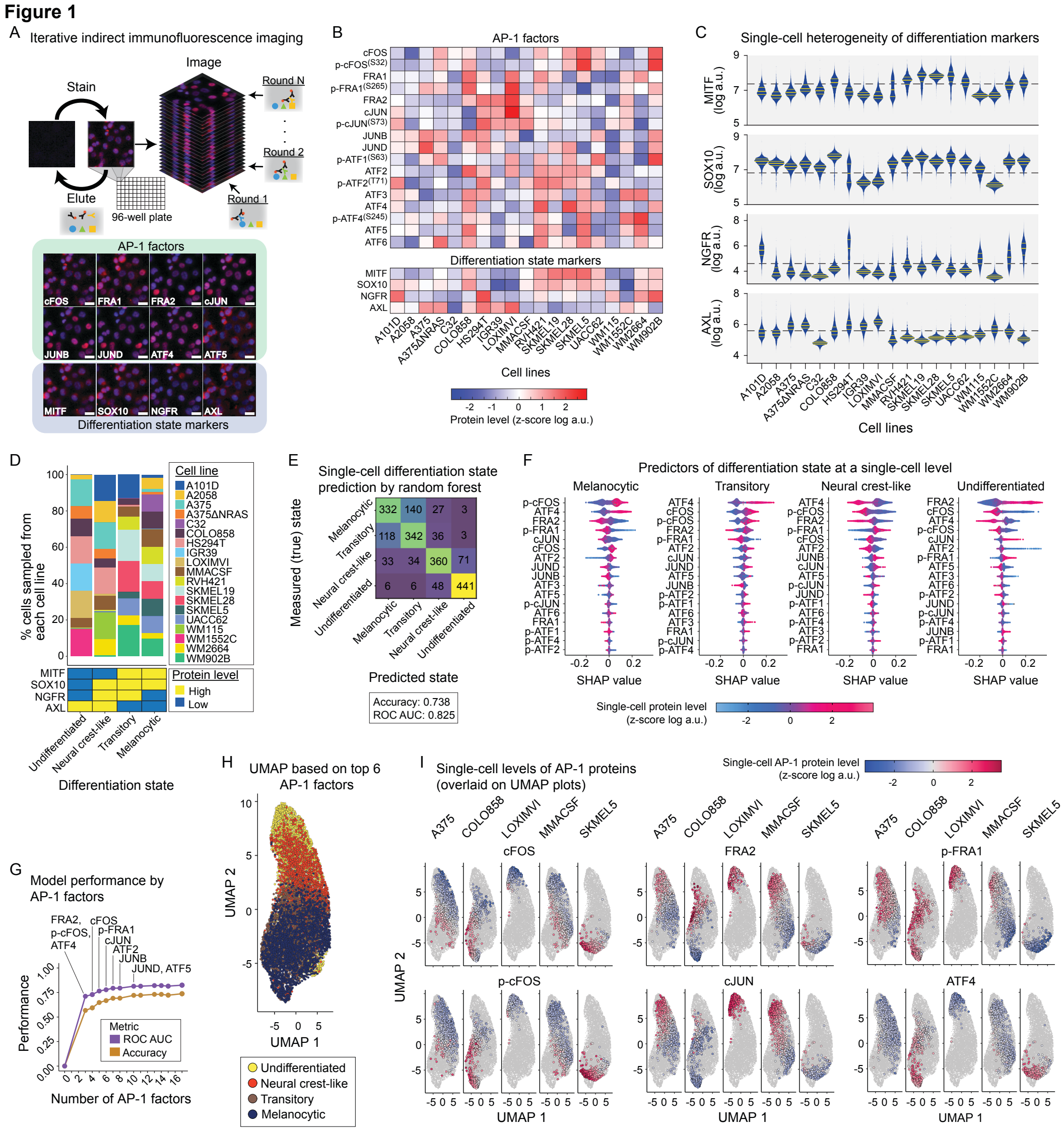
A
Iterative indirect immunofluorescence imaging
Image
Stain
Elute
96-well plate
Round N
Round 2
Round 1
AP-1 factors
cFOS
FRA1
FRA2
cJUN
JUNB
JUND
ATF4
ATF5
MITF
SOX10
NGFR
AXL
Differentiation state markers
B
AP-1 factors
cFOS
p-cFOS(S32)
FRA1
p-FRA1(S265)
FRA2
cJUN
p-cJUN(S73)
JUNB
JUND
p-ATF1(S63)
ATF2
p-ATF2(T71)
ATF3
ATF4
p-ATF4(S245)
ATF5
ATF6
Differentiation state markers
MITF
SOX10
NGFR
AXL
A101D
A2058
A375
A375ΔNRAS
C32
COLO858
HS294T
IGR39
LOXIMVI
MMACSF
RVH421
SKMEL19
SKMEL28
SKMEL5
UACC62
WM115
WM1552C
WM2664
WM902B
Cell lines
-2 -1 0 1 2
Protein level (z-score log a.u.)
C
Single-cell heterogeneity of differentiation markers
MITF (log a.u.)
SOX10 (log a.u.)
NGFR (log a.u.)
AXL (log a.u.)
Cell lines
D
% cells sampled from each cell line
Cell line
A101D
A2058
A375
A375ΔNRAS
C32
COLO858
HS294T
IGR39
LOXIMVI
MMACSF
RVH421
SKMEL19
SKMEL28
SKMEL5
UACC62
WM115
WM1552C
WM2664
WM902B
MITF
SOX10
NGFR
AXL
Protein level
High
Low
Undifferentiated
Neural crest-like
Transitory
Melanocytic
Differentiation state
E
Single-cell differentiation state prediction by random forest
Measured (true) state
Melanocytic 332 140 27 3
Transitory 118 342 36 3
Neural crest-like 33 34 360 71
Undifferentiated 6 6 48 441
Melanocytic
Transitory
Neural crest-like
Undifferentiated
Predicted state
Accuracy: 0.738
ROC AUC: 0.825
F
Predictors of differentiation state at a single-cell level
Melanocytic
Transitory
Neural crest-like
Undifferentiated
SHAP value
Single-cell protein level (z-score log a.u.)
G
Model performance by AP-1 factors
FRA2, p-cFOS, ATF4
cFOS
p-FRA1
cJUN
ATF2
JUNB
JUND, ATF5
Performance
Metric
ROC AUC
Accuracy
Number of AP-1 factors
H
UMAP based on top 6 AP-1 factors
UMAP 2
UMAP 1
Undifferentiated
Neural crest-like
Transitory
Melanocytic
I
Single-cell levels of AP-1 proteins (overlaid on UMAP plots)
Single-cell AP-1 protein level (z-score log a.u.)
A375
COLO858
LOXIMVI
MMACSF
SKMEL5
cFOS
FRA2
p-FRA1
p-cFOS
cJUN
ATF4
UMAP 2
UMAP 1

Figure 2

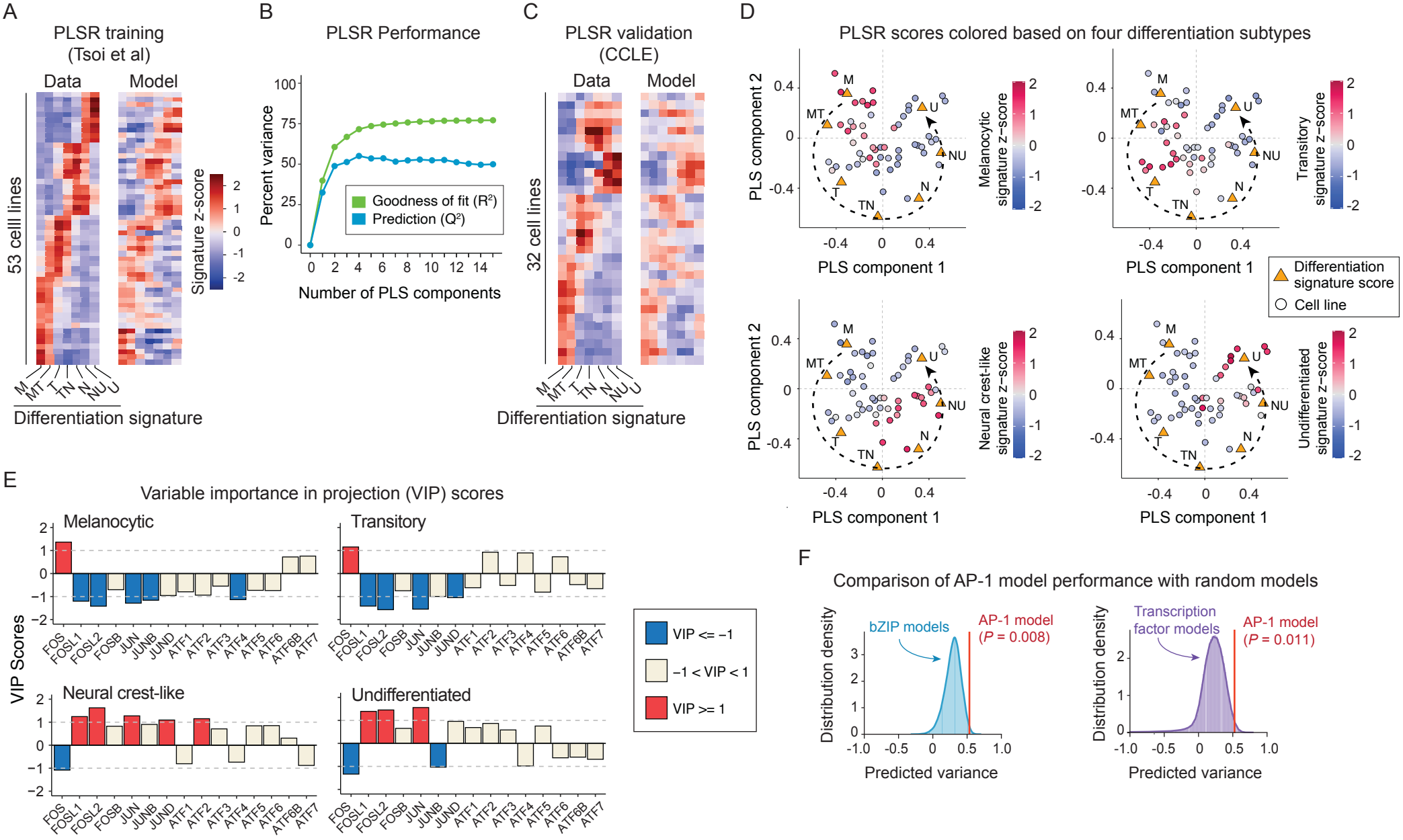
A
PLSR training
(Tsoi et al)
Data
Model
53 celll lines
Signature z-score
M
MT
T
TN
N
NU
U
Differentiation signature
B
PLSR Performance
Percent variance
Goodness of fit (R²)
Prediction (Q²)
Number of PLS components
C
PLSR validation
(CCLE)
Data
Model
32 cell lines
Differentiation signature
D
PLSR scores colored based on four differentiation subtypes
PLS component 2
PLS component 1
Melanocytic signature z-score
Transitory signature z-score
Neural crest-like signature z-score
Undifferentiated signature z-score
Differentiation signature score
Cell line
E
Variable importance in projection (VIP) scores
Melanocytic
Transitory
Neural crest-like
Undifferentiated
VIP Scores
FOS
FOSL1
FOSL2
FOSB
JUN
JUNB
JUND
ATF1
ATF2
ATF3
ATF4
ATF5
ATF6
ATF6B
ATF7
VIP <= −1
−1 < VIP < 1
VIP >= 1
F
Comparison of AP-1 model performance with random models
bZIP models
AP-1 model
(P = 0.008)
Transcription factor models
AP-1 model
(P = 0.011)
Distribution density
Predicted variance

Figure 3

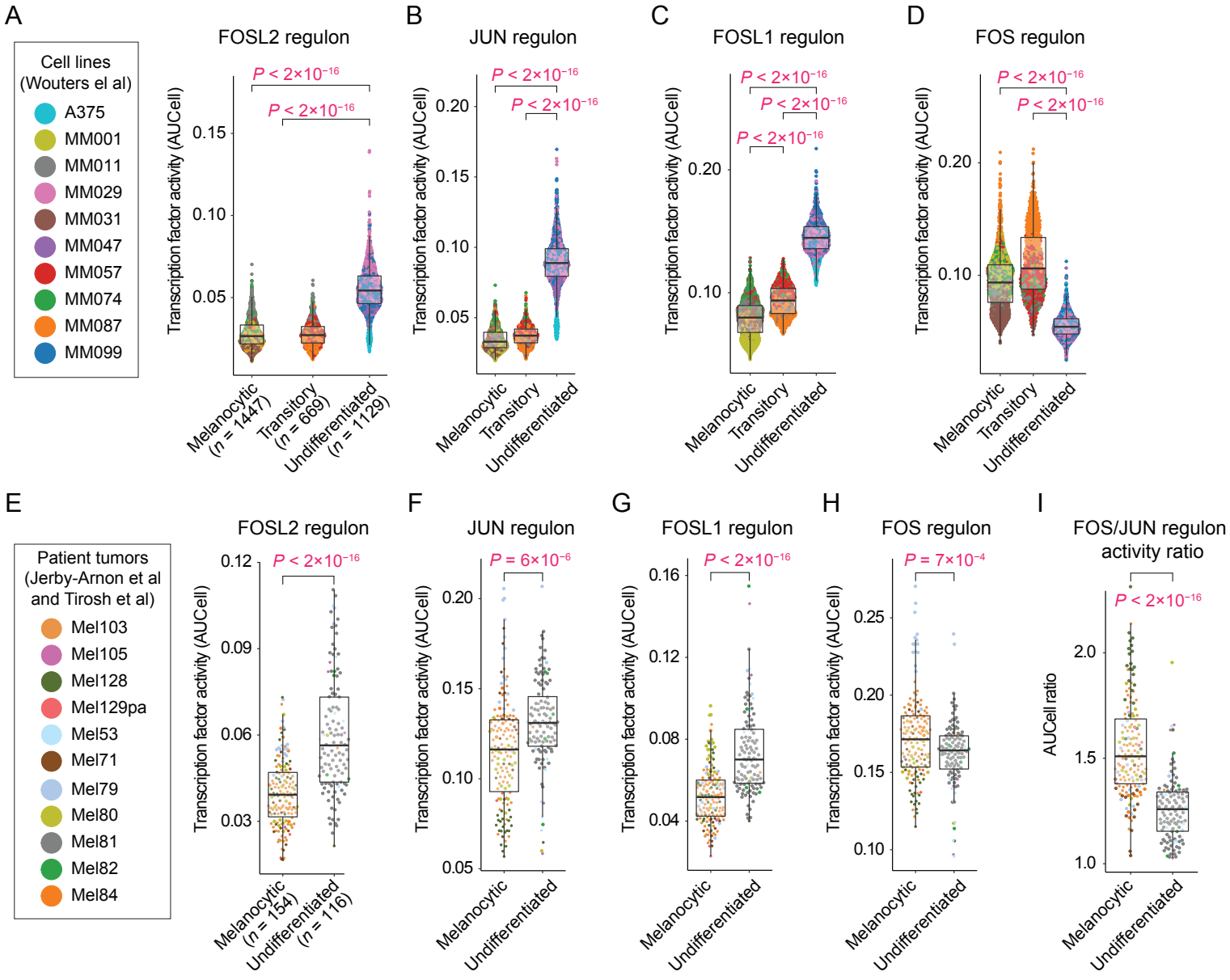
A
Cell lines (Wouters el al)
A375
MM001
MM011
MM029
MM031
MM047
MM057
MM074
MM087
MM099
FOSL2 regulon
Transcription factor activity (AUCell)
P < 2×10−16
P < 2×10−16
Melanocytic (n = 1447)
Transitory (n = 669)
Undifferentiated (n = 1129)
B
JUN regulon
P < 2×10−16
P < 2×10−16
Melanocytic
Transitory
Undifferentiated
C
FOSL1 regulon
P < 2×10−16
P < 2×10−16
P < 2×10−16
D
FOS regulon
P < 2×10−16
P < 2×10−16
E
Patient tumors (Jerby-Arnon et al and Tirosh et al)
Mel103
Mel105
Mel128
Mel129pa
Mel53
Mel71
Mel79
Mel80
Mel81
Mel82
Mel84
FOSL2 regulon
P < 2×10−16
Melanocytic (n = 154)
Undifferentiated (n = 116)
F
JUN regulon
P = 6×10−6
G
FOSL1 regulon
P < 2×10−16
H
FOS regulon
P = 7×10−4
I
FOS/JUN regulon activity ratio
AUCell ratio
P < 2×10−16

Figure 4

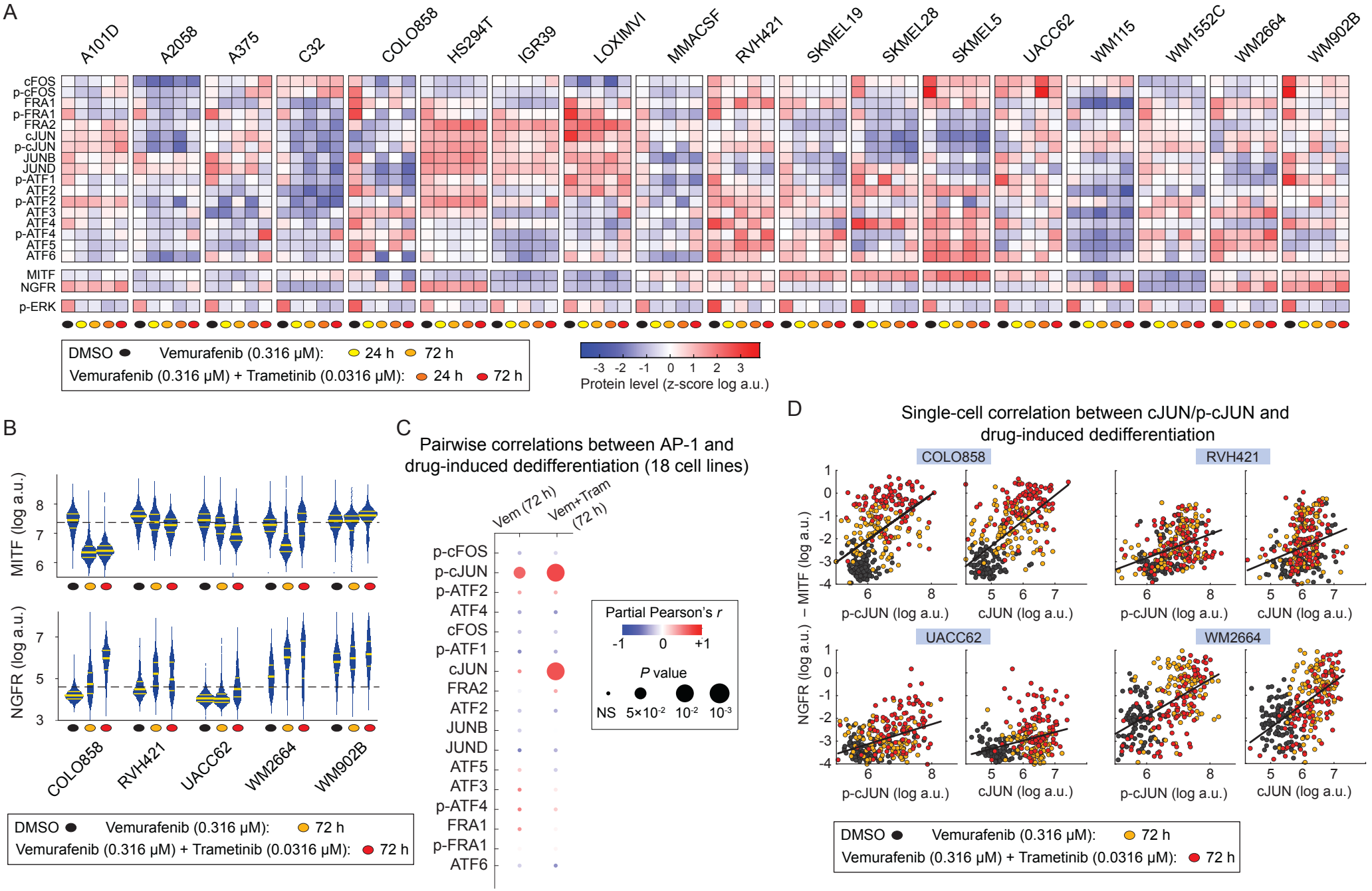
A
A101D
A2058
A375
C32
COLO858
HS294T
IGR39
LOXIMVI
MMACSF
RVH421
SKMEL19
SKMEL28
SKMEL5
UACC62
WM115
WM1552C
WM2664
WM902B
cFOS
p-cFOS
FRA1
p-FRA1
FRA2
cJUN
p-cJUN
JUNB
JUND
p-ATF1
ATF2
p-ATF2
ATF3
ATF4
p-ATF4
ATF5
ATF6
MITF
NGFR
p-ERK
DMSO
Vemurafenib (0.316 μM):
24 h
72 h
Vemurafenib (0.316 μM) + Trametinib (0.0316 μM):
24 h
72 h
-3 -2 -1 0 1 2 3
Protein level (z-score log a.u.)
B
MITF (log a.u.)
NGFR (log a.u.)
COLO858
RVH421
UACC62
WM2664
WM902B
DMSO
Vemurafenib (0.316 μM):
72 h
Vemurafenib (0.316 μM) + Trametinib (0.0316 μM):
72 h
C
Pairwise correlations between AP-1 and drug-induced dedifferentiation (18 cell lines)
Vem (72 h)
Vem+Tram (72 h)
p-cFOS
p-cJUN
p-ATF2
ATF4
cFOS
p-ATF1
cJUN
FRA2
ATF2
JUNB
JUND
ATF5
ATF3
p-ATF4
FRA1
p-FRA1
ATF6
Partial Pearson's r
-1 0 +1
P value
NS 5×10-2 10-2 10-3
D
Single-cell correlation between cJUN/p-cJUN and drug-induced dedifferentiation
COLO858
RVH421
UACC62
WM2664
NGFR (log a.u.) – MITF (log a.u.)
p-cJUN (log a.u.)
cJUN (log a.u.)
DMSO
Vemurafenib (0.316 μM):
72 h
Vemurafenib (0.316 μM) + Trametinib (0.0316 μM):
72 h

Figure 5

A

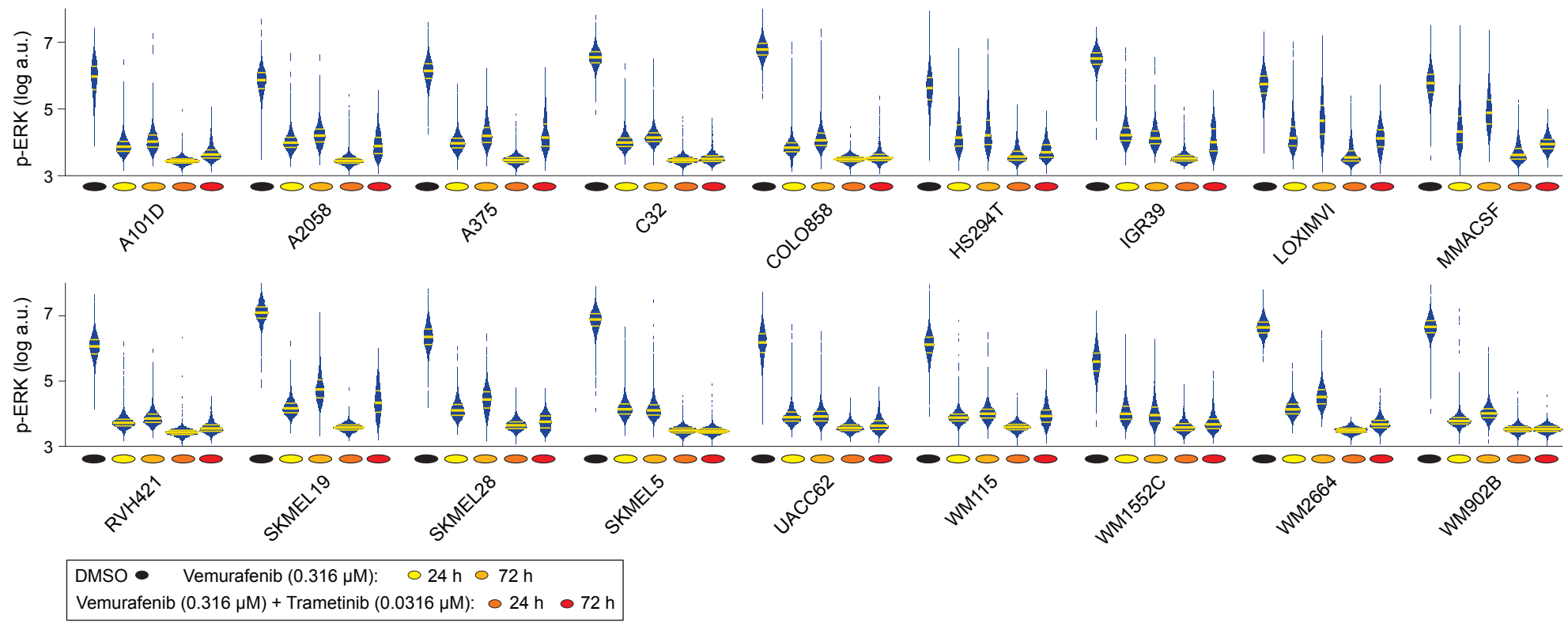

B

Pairwise correlations between AP-1 and p-ERK reactivation (18 cell lines)

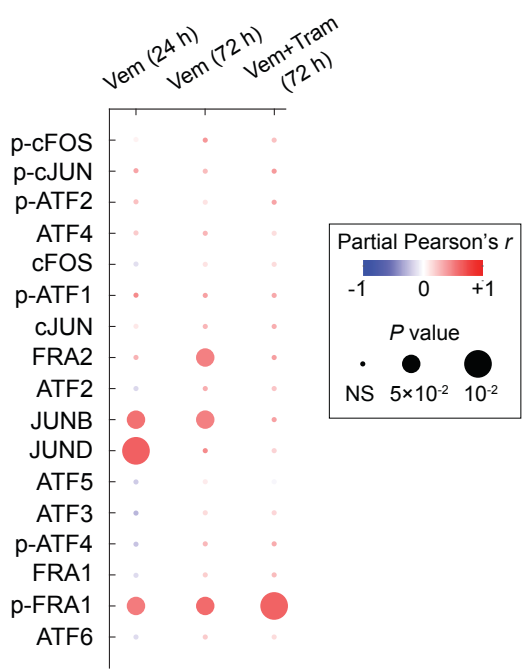

C

Single-cell correlation between p-FRA1 and drug-induced p-ERK changes

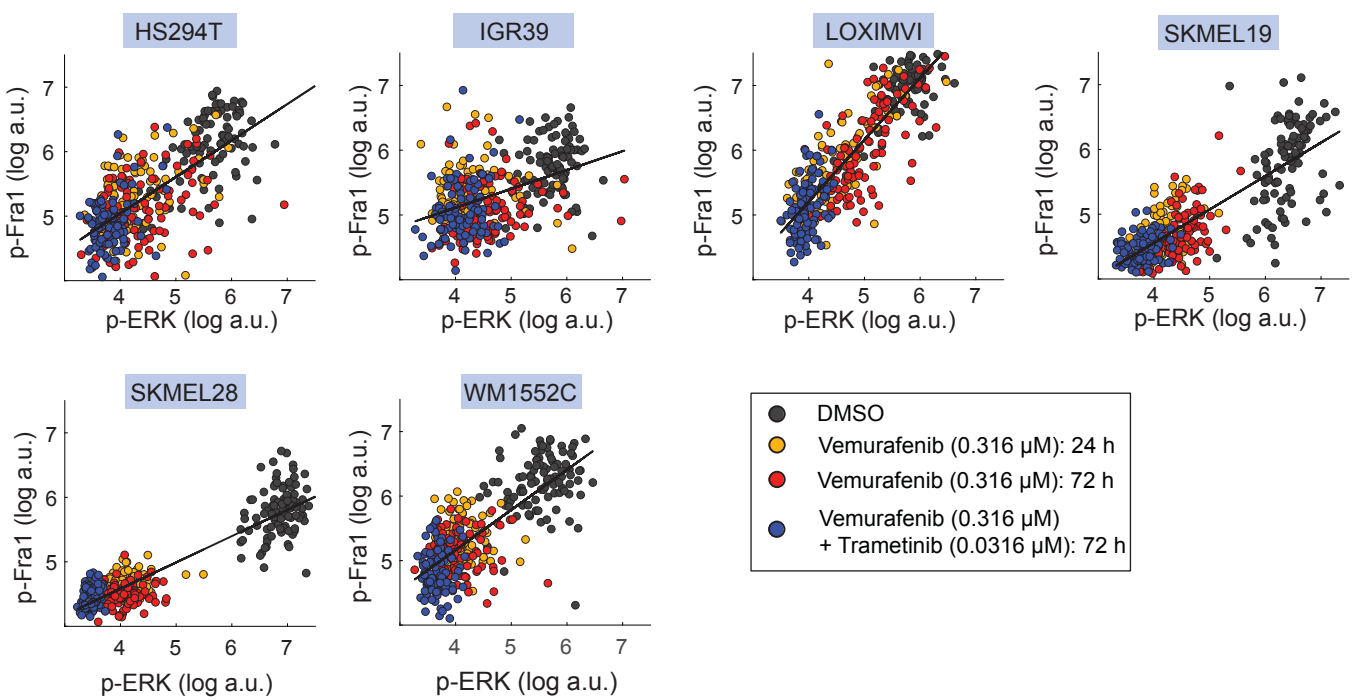

Figure 6

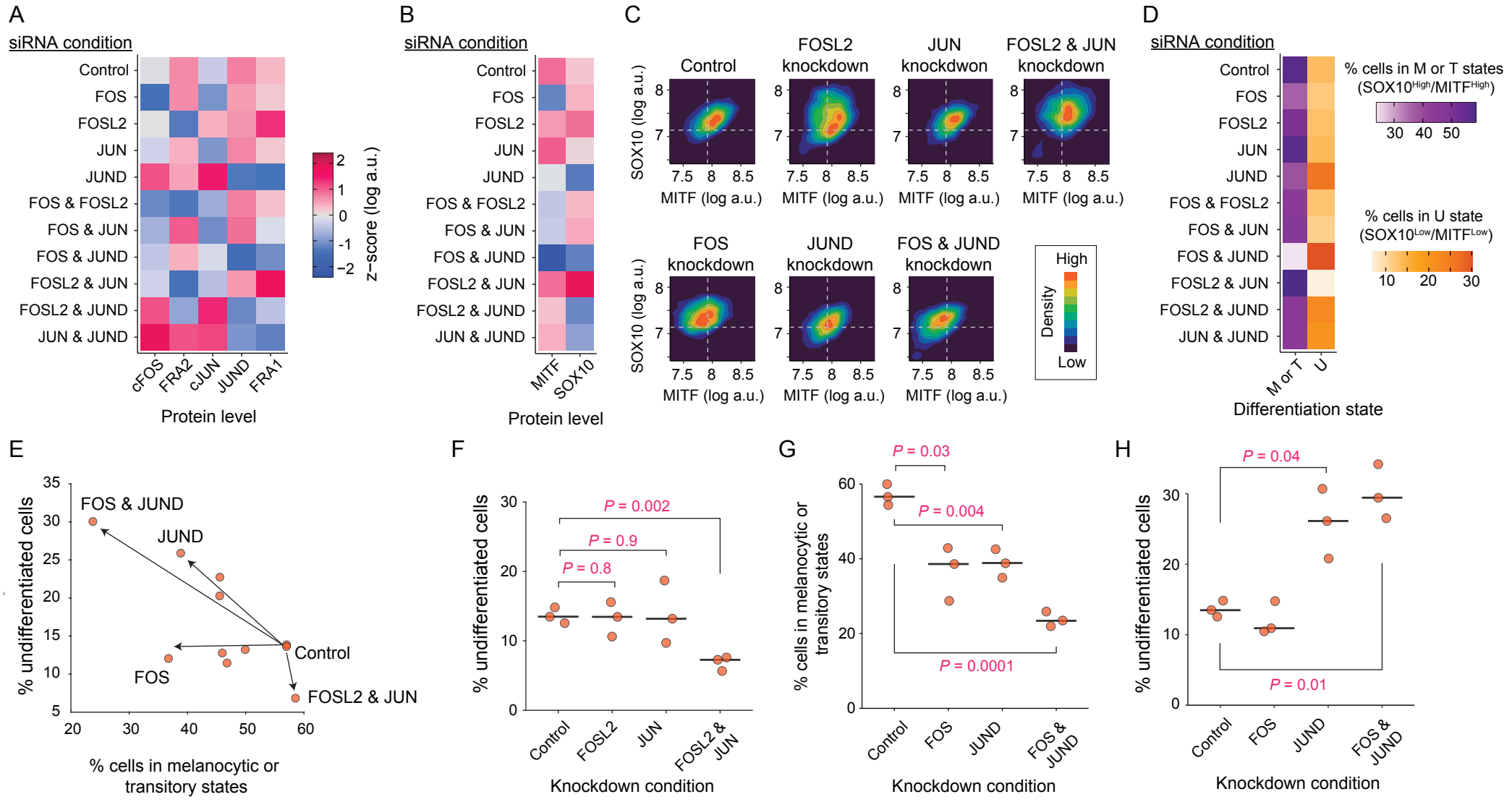
A
siRNA condition
Control
FOS
FOSL2
JUN
JUND
FOS & FOSL2
FOS & JUN
FOS & JUND
FOSL2 & JUN
FOSL2 & JUND
JUN & JUND
cFOS
FRA2
cJUN
JUND
FRA1
Protein level
z−score (log a.u.)
B
siRNA condition
MITF
SOX10
Protein level
C
Control
FOSL2 knockdown
JUN knockdwon
FOSL2 & JUN knockdown
FOS knockdown
JUND knockdown
FOS & JUND knockdown
SOX10 (log a.u.)
MITF (log a.u.)
High
Density
Low
D
siRNA condition
% cells in M or T states (SOX10High/MITFHigh)
% cells in U state (SOX10Low/MITFLow)
M or T
U
Differentiation state
E
FOS & JUND
JUND
Control
FOS
FOSL2 & JUN
% undifferentiated cells
% cells in melanocytic or transitory states
F
P = 0.002
P = 0.9
P = 0.8
% undifferentiated cells
Control
FOSL2
JUN
FOSL2 & JUN
Knockdown condition
G
P = 0.03
P = 0.004
P = 0.0001
% cells in melanocytic or transitory states
Control
FOS
JUND
FOS & JUND
Knockdown condition
H
P = 0.04
P = 0.01
% undifferentiated cells
Control
FOS
JUND
FOS & JUND
Knockdown condition

Figure S1

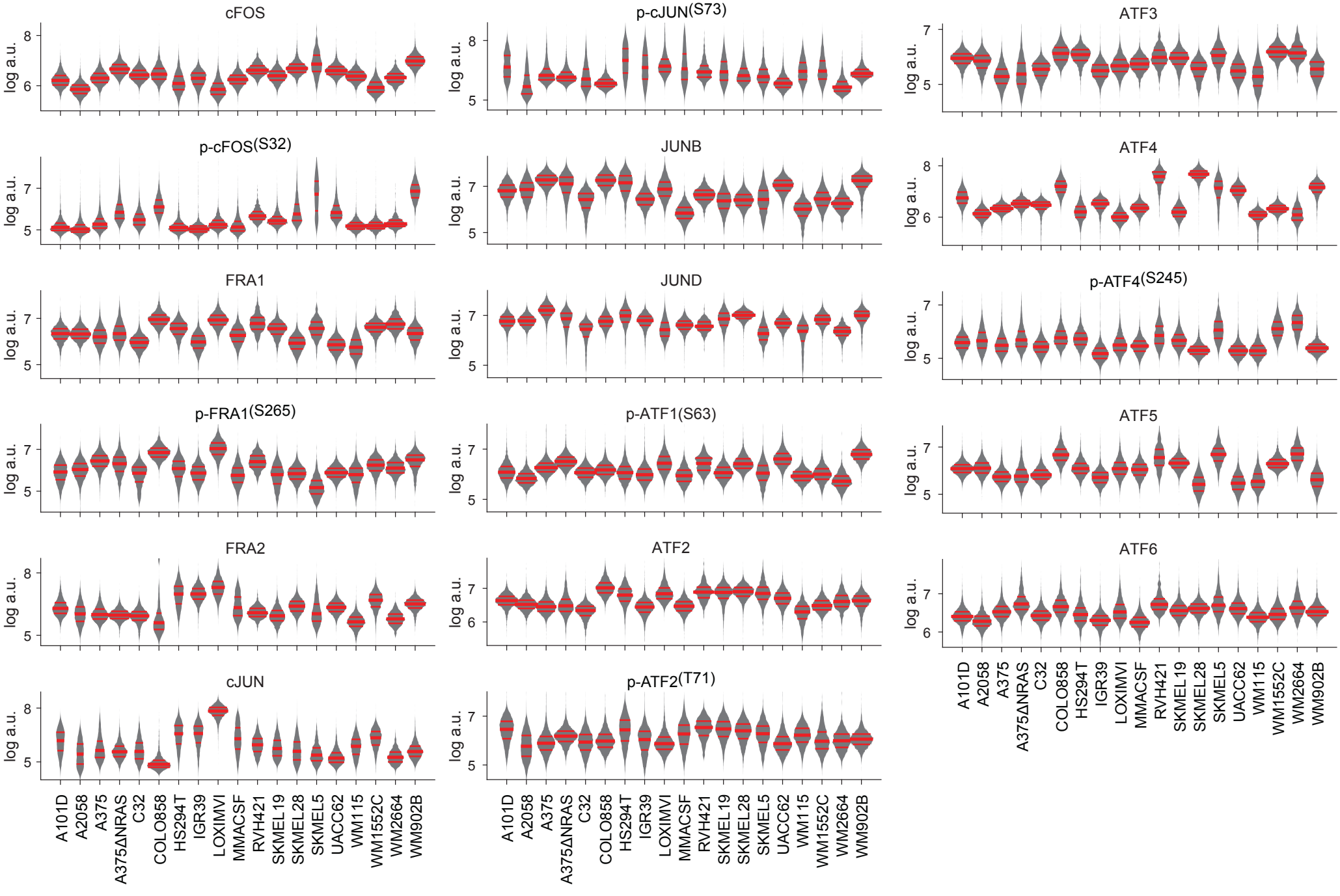
cFOS
p-cJUN(S73)
ATF3
p-cFOS(S32)
JUNB
ATF4
FRA1
JUND
p-ATF4(S245)
p-FRA1(S265)
p-ATF1(S63)
ATF5
FRA2
ATF2
ATF6
cJUN
p-ATF2(T71)
log a.u.
A101D
A2058
A375
A375ΔNRAS
C32
COLO858
HS294T
IGR39
LOXIMVI
MMACSF
RVH421
SKMEL19
SKMEL28
SKMEL5
UACC62
WM115
WM1552C
WM2664
WM902B

Figure S2

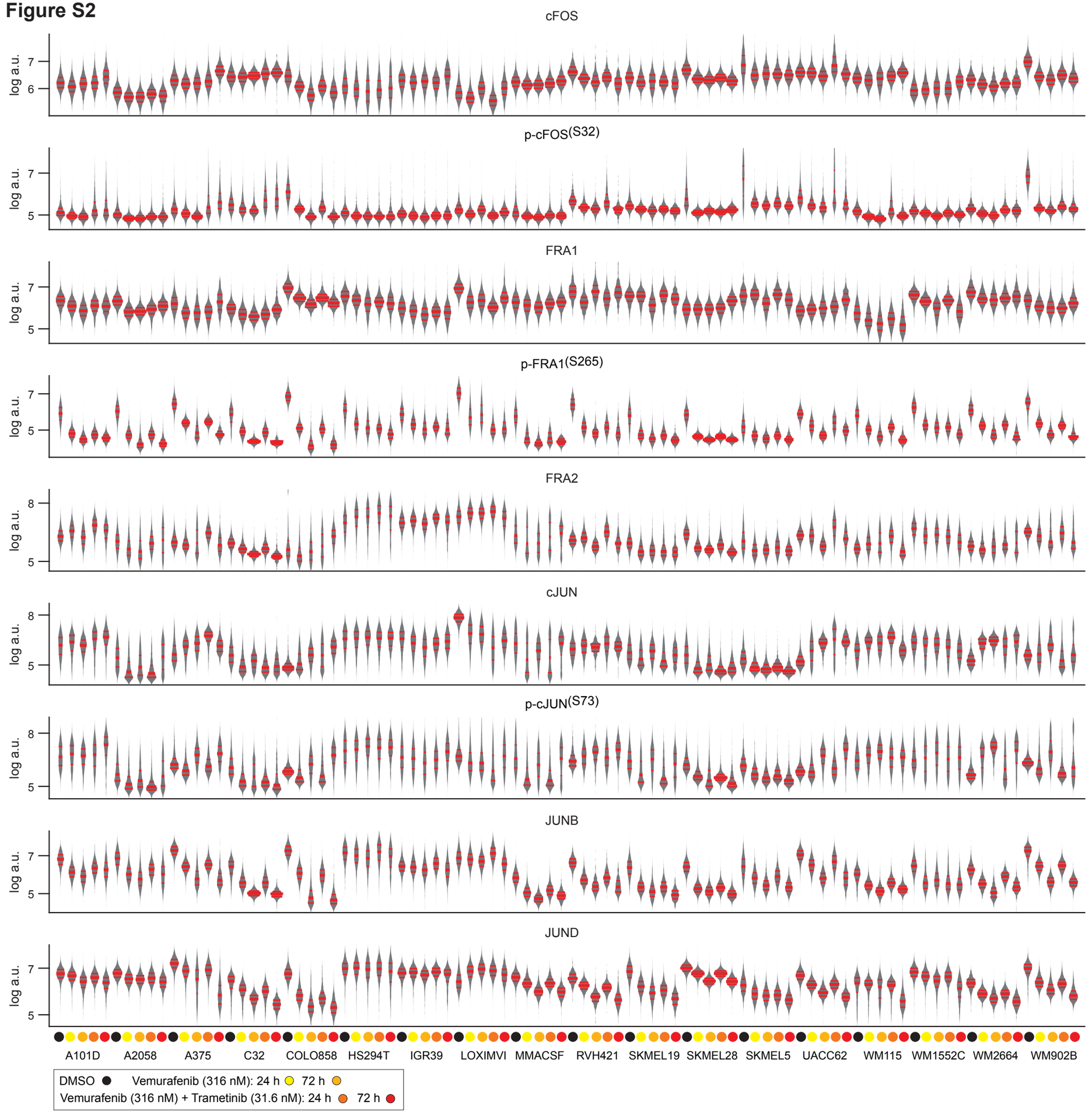
cFOS
p-cFOS(S32)
FRA1
p-FRA1(S265)
FRA2
cJUN
p-cJUN(S73)
JUNB
JUND
log a.u.
A101D
A2058
A375
C32
COLO858
HS294T
IGR39
LOXIMVI
MMACSF
RVH421
SKMEL19
SKMEL28
SKMEL5
UACC62
WM115
WM1552C
WM2664
WM902B
DMSO
Vemurafenib (316 nM): 24 h
72 h
Vemurafenib (316 nM) + Trametinib (31.6 nM): 24 h
72 h

Figure S3

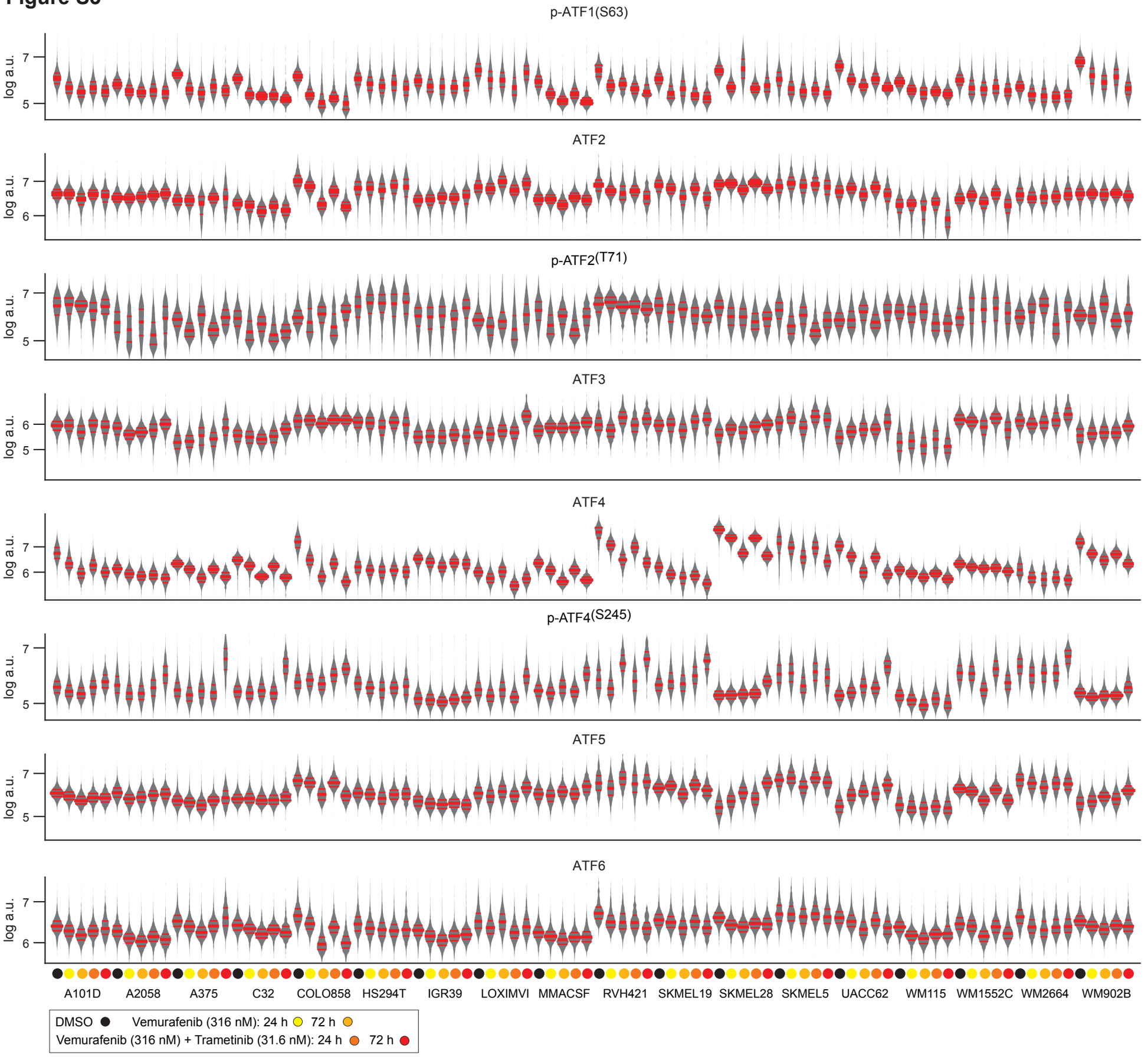
p-ATF1(S63)
ATF2
p-ATF2(T71)
ATF3
ATF4
p-ATF4(S245)
ATF5
ATF6
log a.u.
A101D
A2058
A375
C32
COLO858
HS294T
IGR39
LOXIMVI
MMACSF
RVH421
SKMEL19
SKMEL28
SKMEL5
UACC62
WM115
WM1552C
WM2664
WM902B
DMSO
Vemurafenib (316 nM): 24 h
72 h
Vemurafenib (316 nM) + Trametinib (31.6 nM): 24 h
72 h

Figure S4

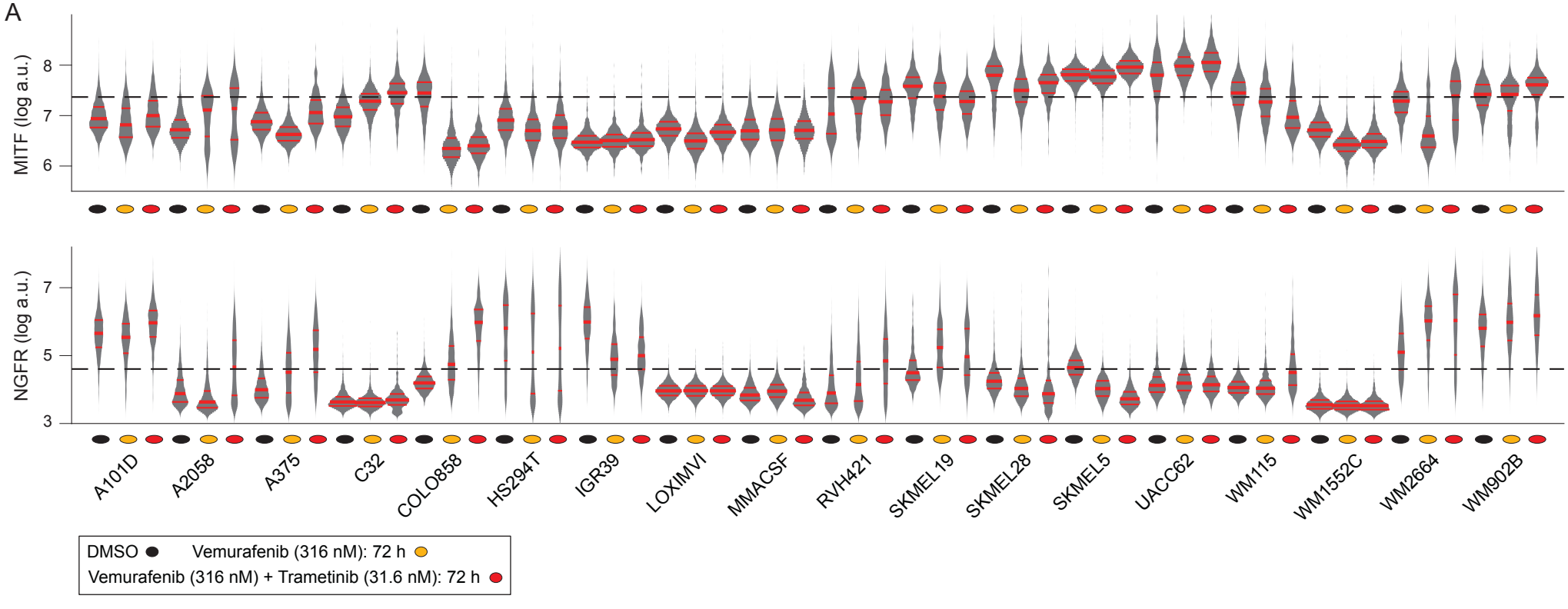
A
MITF (log a.u.)
8
7
6
NGFR (log a.u.)
7
5
3
A101D
A2058
A375
C32
COLO858
HS294T
IGR39
LOXIMVI
MMACSF
RVH421
SKMEL19
SKMEL28
SKMEL5
UACC62
WM115
WM1552C
WM2664
WM902B
DMSO
Vemurafenib (316 nM): 72 h
Vemurafenib (316 nM) + Trametinib (31.6 nM): 72 h